



저작자표시-비영리-변경금지 2.0 대한민국

이용자는 아래의 조건을 따르는 경우에 한하여 자유롭게

- 이 저작물을 복제, 배포, 전송, 전시, 공연 및 방송할 수 있습니다.

다음과 같은 조건을 따라야 합니다:



저작자표시. 귀하는 원저작자를 표시하여야 합니다.



비영리. 귀하는 이 저작물을 영리 목적으로 이용할 수 없습니다.



변경금지. 귀하는 이 저작물을 개작, 변형 또는 가공할 수 없습니다.

- 귀하는, 이 저작물의 재이용이나 배포의 경우, 이 저작물에 적용된 이용허락조건을 명확하게 나타내어야 합니다.
- 저작권자로부터 별도의 허가를 받으면 이러한 조건들은 적용되지 않습니다.

저작권법에 따른 이용자의 권리는 위의 내용에 의하여 영향을 받지 않습니다.

이것은 [이용허락규약\(Legal Code\)](#)을 이해하기 쉽게 요약한 것입니다.

[Disclaimer](#)

Master's Thesis

Cooling Characteristics of Impinging Jet Array and Geometry Optimization

Jaesik Lim

Department of Mechanical Engineering

Graduate School of UNIST

2020

Cooling Characteristics of Impinging Jet Array and Geometry Optimization

Jaesik Lim

Department of Mechanical Engineering

Graduate School of UNIST

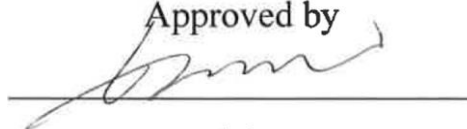
Cooling Characteristics of Impinging Jet Array and Geometry Optimization

A thesis/dissertation
submitted to the Graduate School of UNIST
in partial fulfillment of the
requirements for the degree of
Master of Science

Jaesik Lim

06. 22. 2020 Month/Day/Year of submission

Approved by



Advisor

Jaeseon Lee

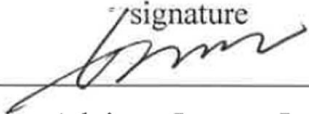
Cooling Characteristics of Impinging Jet Array and Geometry Optimization

Jaesik Lim

This certifies that the thesis/dissertation of Jaesik Lim is approved.

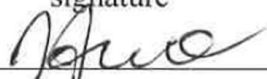
06. 22. 2020 Month/Day/Year of submission

signature



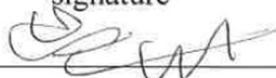
Advisor: Jaeseon Lee

signature



Jae Hwa Lee

signature



Joo Hwan Oh

Abstract

This study deals with two main topics on the cooling characteristics of impinging jets. The first topic, Part I, is the cooling characteristics of impinging jets assisted by the Joule-Thomson effect of carbon dioxide (CO_2). Joule-Thomson effect is the temperature change of real gas when it expands through the nozzle(s) or orifices(s). The CO_2 jet is considered one of the most promising ways to improve the cooling performance due to its superior Joule-Thomson coefficient to other gases. The second topic, Part II, is geometry optimization of array impinging jets and confirmation experiments. The Kriging response surface model and multi-objective genetic algorithm (MOGA) are applied to optimize the impinging jet arrays. The Kriging model is an interpolating technique and suitable for CFD simulation which has a high strength of non-linearity. The objectives of the optimization study are to minimize the average temperature and maximum temperature difference of the target surface. The verification experiments are performed to evaluate the reliability of optimization results. The 3D printing technique is used to build the optimal design of impinging jet arrays. 3D printing has an advantage of fast manufacturing, low cost, and suitable for build a complex structure than conventional manufacturing methods such as machining, casting, and forging.

First of all, in Part I, the cooling characteristics of single and array impinging jets on the flat surface are experimentally investigated with varying Reynolds number (Re_D) and nozzle-to-plate distances (L/D). It is confirmed that the temperature drops of CO_2 and N_2 impinging jets caused by nozzle expansion are about $3.49\text{ }^\circ\text{C}$ and $0.64\text{ }^\circ\text{C}$, respectively. The tendency of stagnation heat transfer coefficients of single impinging jets is consistent with established heat transfer characteristics, but the slightly different trend is shown in this study. There is a maximum value of the stagnation heat transfer coefficient at certain L/D . The value of L/D with the maximum heat transfer coefficient tends to increase as the Re_D increases. The stagnation heat transfer coefficients of CO_2 impinging jet are more sensitive to Re_D increasing than that of N_2 impinging jet, this result is due to the difference of Joule-Thomson coefficients. In case of the same volume flow rate, the heat transfer rates of CO_2 are higher than N_2 . While the performance of uniform cooling by the array impinging jet with CO_2 and N_2 has a similar level, but there is a big difference in the average temperature of the target body. It is beneficial to use the array CO_2 impinging jet to guarantee both high heat transfer coefficient and low temperature non-uniformity.

In Part II, geometry optimization and confirmation experiments are conducted to obtain the enhanced cooling performance of array impinging jets on the flat plate. The central and outer nozzle diameter (d_c and d_o), elliptic nozzle size (a and AR), and jet-to-jet spacing (S) are selected as the design parameters. The lowered average temperature (T_{ave}) and maximum temperature difference (T_{dif}) on

the cooling surface are obtained by using elliptic impinging jet array (EJ). Compared with the initial design, the T_{ave} and T_{dif} are lowered about by 7.6 K and 7.7 % by using the EJ2 jet configuration. The significance of design parameters is evaluated by sensitivity analysis. For the circular impinging jet array (CJ), the d_c and S are major parameters on the T_{ave} and T_{dif} , respectively. In the case of EJ, the value of S is the major parameter for both T_{ave} and T_{dif} . The effects of S/D are analyzed by compared the velocity vector distributions and maximum temperature difference contours. At small S/D , the jet interference that the jets are disturbed by adjacent jets before impinging on the target surface has occurred. The flow characteristics of optimum configurations are evaluated at the location of the jet center and jet interaction. It is confirmed that the axial velocity and turbulent kinetic energy (TKE) distributions of EJ are superior to CJ at the jet interaction region. The 3D printing technique is used to build the optimum design of impinging jet arrays based on the optimization results. Owing to the material properties of the PLA used for 3D printing, the correlations between the CAD design and measured dimensions of the structure are established to predict the shrinking of PLA due to thermal expansion. For all optimum configurations of the impinging jet arrays, the stagnation temperatures decrease as L/D decreases and Re_D increases. The experimental results are matched well with the CFD predictions based on the T_{ave} . Moreover, the order of superior configurations of impinging jet arrays is agreed well with the order EJ2, EJ1, CJ1, and CJ2 of CFD predictions.

Keywords: Jet impingement cooling, Carbon dioxide, Joule-Thomson effect, Temperature uniformity, Geometry optimization, RSM, MOGA, 3D printing

Contents

List of Figures	iii
List of Tables	vi
Nomenclature	vii
1. Introduction	1
2. Joule-Thomson effect	6
3. Part I: Cooling characteristics of single and array impinging jets	8
3.1. Experimental setup and method	8
3.1.1. Experimental apparatus	8
3.1.2. FDM process of 3D printing technique	10
3.1.3. Measurement procedure	12
3.2. Results and discussion	14
3.2.1. Effect of expansion	14
3.2.2. Effect of L/D	15
3.2.3. Effect of Re_D	17
3.2.4. Temperature non-uniformity	20
4. Part II: Geometry optimization and confirmation experiments	21
4.1. Computational details	21

4.1.1. Governing equations	21
4.1.2. Turbulence and near-wall modeling	22
4.1.3. Computational domain and boundary conditions	23
4.1.4. Grid independence test	25
4.2. Optimization strategy	27
4.3. Results and discussion	31
4.3.1. Optimization results	31
4.3.2. Response surfaces	33
4.3.3. Sensitivity analysis	36
4.3.4. Effect of S/D	37
4.3.5. Comparison of flow characteristics	40
4.3.6. 3D printed impinging jet arrays	44
4.3.7. Confirmation experiments	45
5. Conclusions	48
5.1. Part I: Cooling characteristics of single and array impinging jets	48
5.2. Part II: Geometry optimization and confirmation experiments	49
REFERENCES	51

List of figures

Fig. 1. Schematic drawings showing the flow patterns of impinging jet: (a) single impinging jet (b) array impinging jet	5
Fig. 2. Joule-Thomson coefficients of CO ₂ , N ₂ , and H ₂	7
Fig. 3. Schematic of experimental apparatus	8
Fig. 4. Schematics of the (a) test module (b) top view of test section (c) side view of test section	9
Fig. 5. Schematic of an FDM 3D printer	11
Fig. 6. Experimental model of impinging jet nozzle: (a, b) single impinging jet nozzle (c, d) 3D printed impinging jet array nozzle	13
Fig. 7. Comparison of average temperature between steel and 3D printed jet array	13
Fig. 8. Temperature drop of CO ₂ and N ₂ by impinging jet expansion	14
Fig. 9. Stagnation heat transfer coefficient distributions: (a) single CO ₂ impinging jet (b) single N ₂ impinging jet	16
Fig. 10. Stagnation heat transfer coefficient distributions: (a) array CO ₂ impinging jet (b) array N ₂ impinging jet	16
Fig. 11. Stagnation heat transfer coefficients varying with Reynolds number: (a) single CO ₂ impinging jet (b) single N ₂ impinging jet	18
Fig. 12. Stagnation heat transfer coefficients varying with Reynolds number: (a) array CO ₂ impinging jet (b) array N ₂ impinging jet	18

Fig. 13. Stagnation heat transfer coefficients varying with Reynolds number at fixed $L/d=2$: (a) single impinging jet (b) array impinging jet (c) effect of working fluid with varying volume flow rate	19
Fig. 14. Comparative plots showing the temperature non-uniformity of (a) single and array impinging jet (b) array impinging jet with CO_2 and N_2	20
Fig. 15. Schematics of the computational domain and boundary conditions: (a) front view (b) top view (c) CAD rendering image of impinging jet array	24
Fig. 16. The computational domain and grid system	25
Fig. 17. The grid independence test	26
Fig. 18. Schematics of design parameters: (a, b) circular nozzle arranged inline and (c, d) radial outer elliptic nozzle arranged in a different direction	29
Fig. 19. The flow chart of the optimization procedure	30
Fig. 20. The trade-off chart in the optimization process	32
Fig. 21. Response surface plots showing the effects of design parameters for circular jet array: (a, b) the average temperature (c, d) the maximum temperature difference	34
Fig. 22. Response surface plots showing the effects of design parameters for elliptic jet array: (a-d) the average temperature (e-h) the maximum temperature difference	35
Fig. 23. The sensitivity of design parameters for (a) circular jet array (b) elliptic jet array	36
Fig. 24. Velocity vectors with different jet-to-jet spacings: (a) $S/D = 6.0$ (b) $S/D = 15.0$	38
Fig. 25. The maximum temperature difference contours showing the temperature distributions on the cooling surface for the array impinging jets with varying jet-to-jet spacings: (a) $S/D = 6.0$ (b) $S/D = 10.5$ (c) $S/D = 15.0$	39

Fig. 26. Axial velocity and TKE distributions for CJ and EJ at the (a, c) jet center (b, d) jet-to-jet interaction 41

Fig. 27. Axial velocity and TKE distributions for CJ1, CJ2, EJ1, and EJ2 at the (a, c) jet center (b, d) jet-to-jet interaction 42

Fig. 28. Comparison of the 3D streamlines between CJ1 and EJ2 configurations 43

Fig. 29. The 3D printed impinging jet array nozzles of optimum design in CJ1, CJ2, EJ1, and EJ2, respectively 44

Fig. 30. The stagnation temperature distributions with varying L/D : (a) ICJ (b) CJ1 (c) CJ2 (d) EJ1 (e) EJ2 46

Fig. 31. The effects of Re_D on the stagnation temperature 47

Fig. 32. The comparison between CFD predictions and experiment results: (a) average temperature (b) maximum temperature difference 47

List of tables

Table 1. Thermodynamic properties of working fluid	7
Table 2. FDM process parameters and values for 3D printing	11
Table 3. The optimization results based on MOGA approach	32

Nomenclature

<i>Symbol</i>	<i>Description</i>	<i>Unit</i>
L	Nozzle-to-plate distance	[<i>mm</i>]
H	Enthalpy	[<i>kJ/kg</i>]
l_1, l_2	Horizontal distances between the thermocouples	[<i>mm</i>]
z_1, z_2	Vertical distances between the thermocouples	[<i>mm</i>]
T	Temperature	[<i>K, °C</i>]
ΔT	Temperature difference of stagnation point and nozzle inlet	[<i>K, °C</i>]
d	Nozzle hole diameter	[<i>mm</i>]
D	Equivalent diameter of jet array	[<i>mm</i>]
Re_D	Reynolds number based on D	[-]
V	Volume	[<i>m³</i>]
V_j	Velocity at the jet inlet	[<i>m/s</i>]
P	Pressure	[<i>MPa, bar</i>]
U	Internal energy	[<i>J</i>]
R^2	Coefficient of determination	[-]
NPR	Nozzle pressure ratio	[-]
q''	Heat flux	[<i>W/m²</i>]
C_p	Specific heat	[<i>J/kg · K</i>]
S	Jet-to-jet spacing	[<i>mm</i>]
y^+	Dimensionless distance	[-]
y_p	Height of the first cell	[<i>mm</i>]
d_c	Diameter of nozzle at the central of jet array	[<i>mm</i>]

d_o	Diameter of nozzles at the outer of jet array	[mm]
$C_1, C_2, C_{1\varepsilon}, C_{3\varepsilon}$	Empirical constants in turbulence model	[-]
x, y, z	Coordinate system	[mm]
u_i, u_j	Arbitrary velocity components	[m/s]
a	Minor axis length of elliptic nozzle	[mm]
AR	Aspect ratio of minor and major axis length	[-]
b	Major axis length of elliptic nozzle	[mm]
τ_w	Wall shear stress	[Pa]
v	Axial velocity	[m/s]
Pr_t	Turbulent Prandtl number	[-]
u_τ	Shear velocity	[m/s]
U_i, U_j	Time averaged velocity components	[m/s]
Re_y	Turbulent Reynolds number	[-]
S_k, S_ε	User-defined source terms	[-]

Greek

μ_{JT}	Joule-Thomson coefficient	[K/MPa]
μ_t	Turbulent viscosity	[m ² /s]
ρ	Density	[kg/m ³]
μ	Dynamic viscosity	[kg/m · s]
λ	Thermal conductivity	[W/m · K]
k	Turbulence kinetic energy	[m ² /s ²]
ν	Kinematic viscosity	[m ² /s]
ε	Turbulence dissipation rate	[m ² /s ³]

$\sigma_k, \sigma_\varepsilon$	Turbulent Prandtl numbers based on k and ε	[-]
δ_{ij}	Kronecker delta	[-]
Γ, Π	Near-wall blending functions	[-]
α, β	Constants for the blending function	[-]

Subscript

<i>ave</i>	Average value
<i>max</i>	Maximum value
<i>min</i>	Minimum value
<i>in</i>	Nozzle inlet
<i>s</i>	Surface
<i>dif</i>	Maximum difference
<i>measure</i>	Measured dimension
<i>design</i>	Designed dimension

Superscript

—	Mean
'	Fluctuation
+	Dimensionless value

Abbreviation

<i>MOGA</i>	Multi-Objective Genetic Algorithm
<i>RSM</i>	Response Surface Methodology
<i>CFD</i>	Computational Fluid Dynamics

<i>EWT</i>	Enhanced Wall Treatment
<i>DX</i>	DesignXplorer
<i>CAD</i>	Computational Aided Design
<i>FDM</i>	Fused Deposition Modeling
<i>RANS</i>	Reynolds averaged Navier-Stokes
<i>DoE</i>	Design of Experiment
<i>CCD</i>	Central Composite Design
<i>TKE</i>	Turbulent Kinetic Energy
<i>DSP</i>	Decision Support Process
<i>ICJ</i>	Initial Circular impinging Jet array
<i>CJ</i>	Circular impinging Jet array
<i>EJ</i>	Elliptic impinging Jet array
<i>NSGA-II</i>	Non-dominated Sorted Genetic Algorithm-II
<i>FDM</i>	Fused Deposition Modeling
<i>PLA</i>	Polylactic Acid

1. Introduction

Jet impingement is a technique for ejecting a flow of high momentum issued from a nozzle(s) or orifice(s) onto a target surface. Impinging jet has been a well-established technique as a localized heating, cooling, and drying to various industrial applications, such as cooling of the electronic systems or gas turbine blade, tempering of glass, food processing, and drying of textiles [1-8]. Due to its ability to high heat and mass transfer, it has been received significant attention form many researchers. In general, the uniform temperature of a solid surface is a key design parameter of some applications such as electronic components and batteries, as non-uniform surface temperature leads to the thermal shock or defect which reduces the life of the applications [9]. Therefore, studies on the thermal effects of impinging jets on the application components in the industrial fields have been continuously demanded, so many researchers have been broadly investigated the flow and heat transfer characteristics of impinging jets.

Fig. 1 shows the flow regions of the single and array impinging jet. For a single impinging jet, there are generally divided into four regions: (1) the free jet region, (2) the potential core region, (3) the stagnation region, and (4) the wall jet region. In the free jet region, the jet flow begins decelerated and broaden due to the entrainment of mass, momentum, and energy of the surrounding fluid. The region which is not affected by shear-driven interaction of surrounding fluid and approximately equal to the nozzle outlet velocity is potential core. The stagnation region is the impinging zone that jet forms a high static pressure on the target surface, and then the velocity profiles are converted to the accelerated horizontal components and it grows into wall jet region. While the single impinging jet yields a superior heat transfer rate near the impingement region, it drops dramatically as away from the stagnation region [10]. As a result, the temperature uniformity of the target body cooled by the single impinging jets is poor. Compared to the single impinging jet, the array impinging jets have a fountain flow region due to the wall jet collisions. For the array impinging jet, there is shear layer expansion due to the jet-to-jet interactions, resulting in more uniform temperature distributions of the cooling surface than the single impinging jet [11]. Therefore, the array impinging jet is regarded as a promising way to ensure the uniform cooling performance.

As the demand for enhanced cooling performance increases in many industrial applications, the cooling characteristics of single and array impinging jets have been broadly investigated. Gauntner et al. [12] have shown the length of potential core was 4.7 to 7.7 nozzle diameters based on the survey. Katoka [13] proposed the correlation of potential core length and showed that the peak heat transfer coefficient was obtained at the end of potential core. Guo et al. [14] investigated the flow visualization for wall jet development in confined impinging jet using the stereo particle image velocimetry method.

They observed that the counterclockwise vortex structure interrupts the wall jet development at the small L/D . Katti et al. [15] investigated the local heat transfer coefficient distributions. They suggested the correlations for predicting the local Nusselt number. Yang et al. [16] investigated the heat transfer characteristics of array impinging jets on the concave surface. They showed that the maximum heat transfer rates appeared at $L/D = 10$ and S/D is the significant factor for the array impinging jet. Xing et al. [18] studied the cooling performance of impinging jet arrays which inline and staggered array nozzles with varying Reynold numbers. They showed that the highest heat transfer coefficient was obtained at $L/D = 3$ and the inline configuration always outperformed the staggered pattern. San et al. [17] investigated the Nusselt number distributions of array impinging jets. They have shown that the major and minor parameters to affect the non-uniformity of heat transfer distributions are S/D and L/D , respectively. Wae-hayee et al. [19] studied the cooling characteristics of array impinging jets under a fully developed flow. They revealed that the peak of average heat transfer rate occurred at $L/D = 4$ over all S/D .

Meanwhile, the effects of nozzle geometry on the heat transfer have also been focused on many researchers. Dano et al. [20] described the heat transfer characteristics of impinging jet arrays including conventional circular and ellipse nozzles. They found that the improved heat transfer rates and uniformity can be obtained by using the elliptic nozzles. Culun et al. [21] numerically investigated the effects of design factors on the flow and cooling characteristics. They revealed that the improved heat transfer rates achieved in the case of square jets due to the higher mixing flow. Caliskan et al. [22] studied the effects of nozzle geometries on the array impinging jet heat transfer. They measured the heat transfer rates and velocity profiles of impinging jet arrays for aspect ratios (AR) 0.5, 1.0, and 2.0. The results show that the elliptic jet with aspect ratio 2.0 yields the highest heat transfer rates than other jet configurations. Attalla et al. [14] studied the heat transfer uniformity of the inline array of impinging jets. They suggested the correlations of heat transfer uniformity and concluded the uniform cooling performance was achieved by the square nozzle configurations. Lee et al. [24] studied the Nusselt number distributions of elliptic impinging jets with varying the aspect ratio (AR) 1.0 to 4.0. They observed that the maximum heat transfer rate can be obtained using the elliptic impinging jet due to its azimuthal curvature variations of the vortical structure. Gulati et al. [25] experimentally investigated the comparison study for rectangular, square, and circular nozzle configurations with varying L/D and Reynolds number. They revealed that the Nusselt number distributions of the elliptic impinging jet were higher than circular and square nozzle configurations within the range of 6 L/d and the pressure loss coefficient is highest. Koseoglu et al. [26] investigated the circular, rectangular, and elliptic jets with different aspect ratio. In the condition of the same mass flow rate, as aspect ratio increases, the heat transfer rate enhanced in the stagnation region and decreases in the wall jet region.

Due to the need for enhanced cooling performance of the impinging jet, various kinds of working fluids for jet impingement have been considered. Zhang et al. [27] experimentally investigated the liquid nitrogen (N_2) jets. In general, the liquid impinging jet has a higher heat transfer rate than the gas impinging jet. However, liquid impinging jets need to the recirculation system to recycle the exhausted working fluid and difficult to apply to moisture-sensitive applications. While gas impinging jets inferior heat transfer rate to liquid impinging jets, it does not need additional costs to the closed-loop system and can be applied to various applications. Therefore, there is a continuous demand for the study of impinging jets for different kinds of gas types to enhance the heat transfer rate. The carbon dioxide (CO_2) jet is considered one of the most promising ways for heat transfer improvement due to its superior Joule-Thomson coefficient to other gases. As gases ejected through the nozzle, its pressure and temperature are drops simultaneously due to the Joule-Thomson effect. Namely, the CO_2 impinging jet has a potential to improve heat transfer performance than the impinging jet using other gases [28,29].

On one hand, some researchers were focused on the geometry optimization of the impinging jet array. Chi et al. [30] built a novel system of impingement cooling geometry with variable diameter nozzle holes by using multi-objective genetic algorithms (MOGA). Chiang [31] proposed the effective optimization procedure for thermal performance characteristics of the confined impinging jet over parallel plain fin structures by using the response surface methodology (RSM). Heo et al. [32] investigated the geometry optimization of a single impinging jet with crossflow. They revealed that the average heat transfer rates number on the cooling surface was enhanced by about 7.89 % as compared to the initial geometry.

On the other hand, some investigators studied impinging jets by using the 3D printing technique due to its ability to customize and good stability. Fernandes et al. [33] proposed the tunable diameter of the nozzle assembly for micro liquid impinging jet by using the 3D printing technique. They concluded that this nozzle assembly can be applied to many industrial fields to build their own system. Masuk et al. [34] investigated the dynamics of multiphase flow by using the 3D printed jet array. They described the 3D printing technique was the best option for establishing the cooling system due to the 3D printed jet array has a waterproof and strong enough to endure the high-pressure condition. Shankar et al. [35] experimentally investigated the swirl impinging jet via the 3D printed swirl generators. Wei et al. [36] proposed the scalable design methodology for the 3D printed impinging jet arrays. They suggested that the 3D printing technique has an advantage of the capabilities to build the complex structures and high-resolution stereolithography with the water-resistant.

As can be seen in the paper reviews, most of the previous studies were focused on the effects of geometric parameters on the flow and heat transfer characteristics of single and array impinging jets by using compressed air. However, there was not much information was available on the enhancement of the cooling performance of single and array jets assisted by the Joule-Thomson effect of CO₂. Furthermore, there were few studies on the combined investigation that the geometry optimization of the impinging jet array and confirmation experiments of optimization results. The purpose of the present study is to investigate the cooling characteristics of single and array impinging jets. To confirm the Joule-Thomson effect, the CO₂ and N₂ are selected as the working fluid. This is covered in Part I. Part II deals with a numerical investigation to find the optimal designs of impinging jet arrays. The optimization is performed by RSM and MOGA approach. And then, the verification of optimization results is experimentally investigated. The 3D printing technique is used to fabricate the optimum design of impinging jet arrays. In Part II, the methodological research method is presented for verifying optimization results using 3D printing, an easy, low cost, and fast manufacturing method.

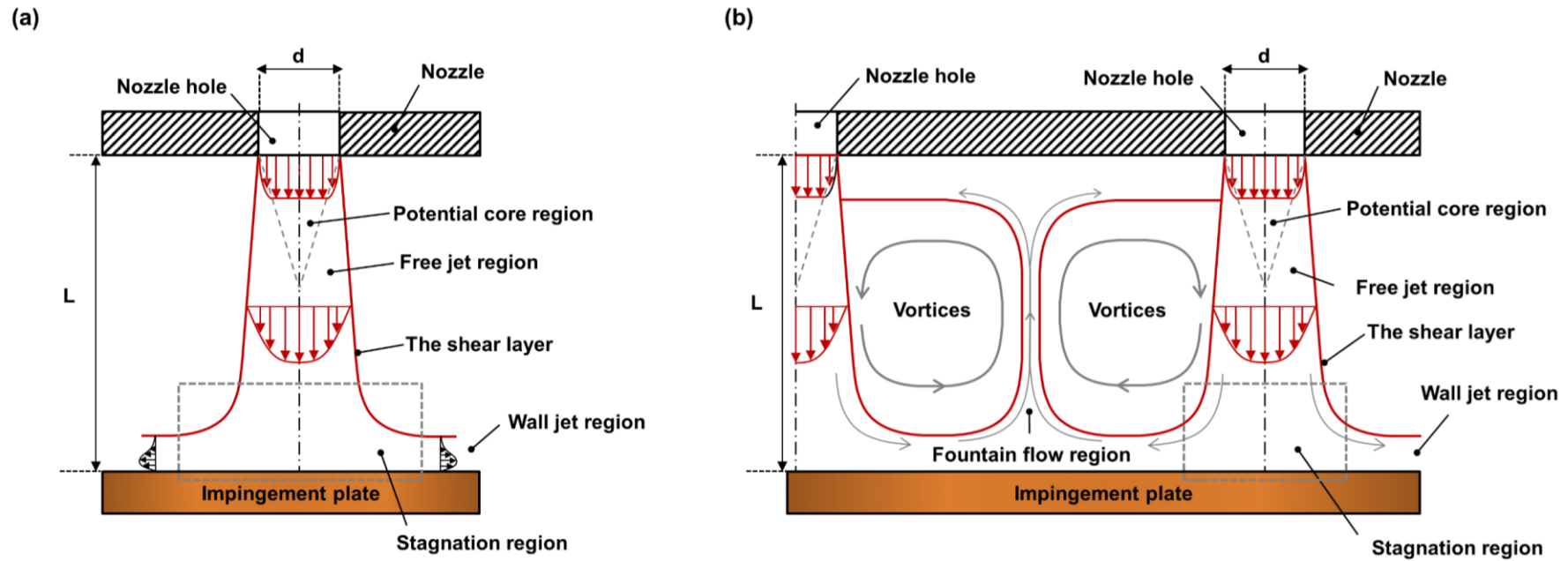


Fig. 1. Schematic drawings showing the flow patterns of impinging jet: (a) single impinging jet (b) array impinging jet.

2. Joule-Thomson effect

As previously described, jet impingement cooling via CO₂ impinging jet has a superior to heat transfer performance than other gases jet due to the difference of the Joule-Thomson coefficient. Joule-Thomson effect is the temperature drop of real gas when it expands through the nozzle(s) or orifices(s). The Joule-Thomson expansion is called a throttling process, a condition that is thermally insulated so that no heat is exchanged with the ambient.

$$\Delta H = \Delta U + \Delta PV \quad (1)$$

There are two mechanisms of the temperature change of gases through the Joule-Thomson expansion. The first one is the change of internal energy and the second one is the conversion between potential and kinetic energy. The temperature change means a variance of kinetic energy and internal energy is defined as the sum of potential and kinetic energy. The change of enthalpy in the Joule-Thomson expansion is shown in Eq. (1), and enthalpy remains constant in the throttling process. The value of PV does change for a real gas, so there is a variance of temperature due to changes in internal energy. If the PV decreases, the temperature increases due to the increases of internal energy, this phenomenon is called a negative Joule-Thomson effect. On the contrary, an increase in PV causes a temperature drop, which is called a positive Joule-Thomson effect. Also, there are the effects of intermolecular conditions in the change of temperature. When the fluid expands through the nozzle, the potential energy of fluid increases due to the force of attraction between the molecules or decreases due to the reduces in the number of the molecular collision. These two mechanisms are occurred simultaneously, the temperature decreases for the former case, increases for the latter case. At room temperature, the temperature of CO₂ and N₂ decreases through the expansion and the temperature of He and Ne increases through the expansion [37].

$$\mu_{JT} = \left(\frac{\partial T}{\partial P}\right)_H \quad (2)$$

Fig. 2 shows the Joule-Thomson coefficients of real gases at atmospheric pressure. The Joule-Thomson coefficient is defined as the ratio of the variance of temperature and pressure, as can be seen in Eq. (2). The Joule-Thomson coefficient of CO₂ is superior to N₂, and H₂. Therefore, the temperature drops of CO₂ is dramatic than other gases if the pressure drop is the same amount. As a result, the cooling benefits can be obtained by using the CO₂ impinging jet. The N₂ impinging jet is investigated to compare the cooling performance. Table 1 show the thermodynamic properties of CO₂ and N₂ at atmospheric pressure and 296.15 K, which values are obtained from REFPROP [38].

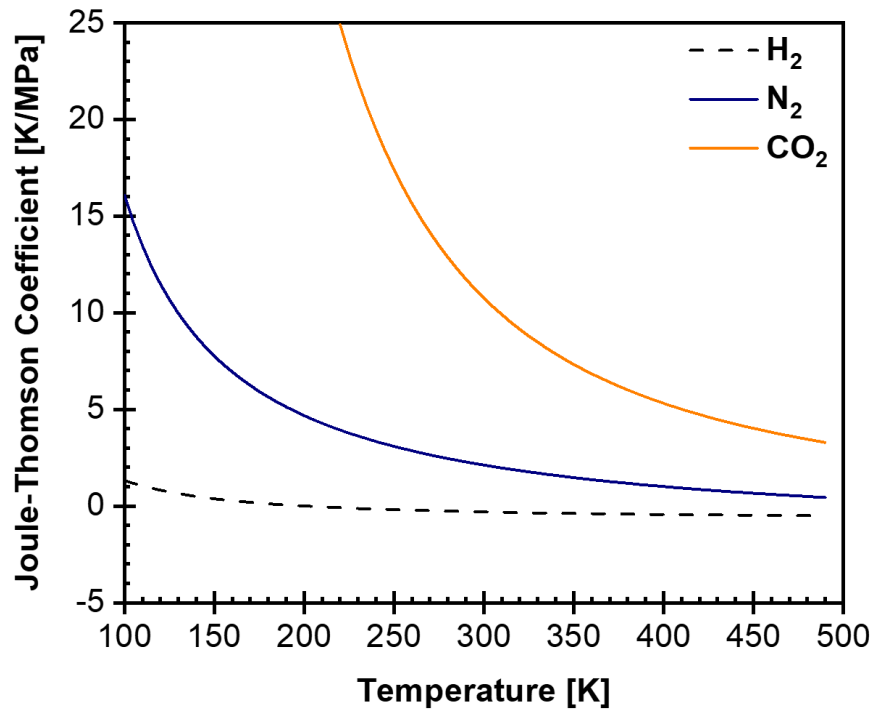


Fig. 2. Joule-Thomson coefficients of CO₂, N₂, and H₂ .

Table 1. Thermodynamic properties of working fluid.

Gas	Density [kg/m ³]	Joule-Thomson Coefficient [K/MPa]	Specific heat [kJ/kg · K]	Viscosity [μPa · s]	Thermal conductivity [mW/m · K]
CO ₂	1.8204	11.122	0.8489	14.835	16.482
N ₂	1.1530	2.180	1.0413	17.712	25.690

3. Part I: Cooling characteristics of single and array impinging jets

3.1. Experimental setup and method

3.1.1. Experimental apparatus

The experimental apparatus including, a filter, valve, flow meter, nozzle assembly, test section, AC power supply, power meter, and data acquisition system is shown in Fig. 3. The compressed CO_2 and N_2 supplied from the gas cylinder, and the pressure is high enough to expand into the ambient air. The filter ensures the high purity working fluid, and the volume flow rate is controlled and monitored by the control valve and mass flow meter. The pressure transducer and T-type thermocouples are inserted in the location of the nozzle inlet to measure the absolute pressure and temperature. The test body is heated a fixed power 20W by the voltage variable transformer and the heating power is monitored by a power meter. All the signals from the flow meter, pressure transducer, and thermocouples are processed by a data acquisition system.

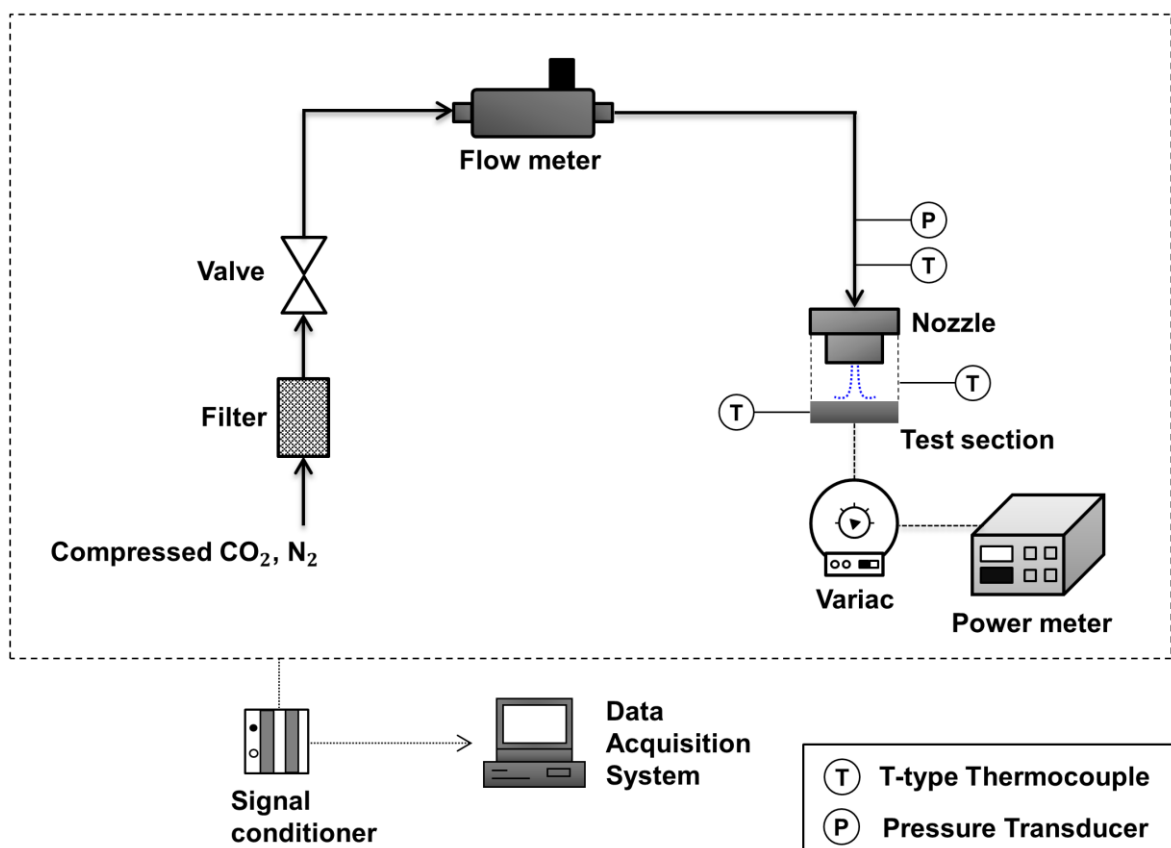


Fig. 3. Schematic of experimental apparatus.

Fig. 4 shows the detailed descriptions of the impinging jet cooling system and test section. The jet fluid supplied to the plenum of the nozzle assembly and ejected onto the target surface. The test section is made of aluminum alloy of 55 mm × 55 mm × 15 mm. The heater consists of the copper block which inserted cartridge rods. The insulation material is installed around the heater, test section, and impinging jet array to preventing the heat losses to the ambient. The nozzle-to-plate distance (L) is controlled by a z-axis stage installed under the impinging jet cooling system. As described in Fig. 4(b) and (c), the eight thermocouples are inserted in the test section to measure the local temperature of the test section. The thermocouples are aligned at distances of $l_1 = 15.0$ mm, $l_2 = 7.5$ mm, $z_1 = 3$ mm, and $z_2 = 6$ mm, respectively.

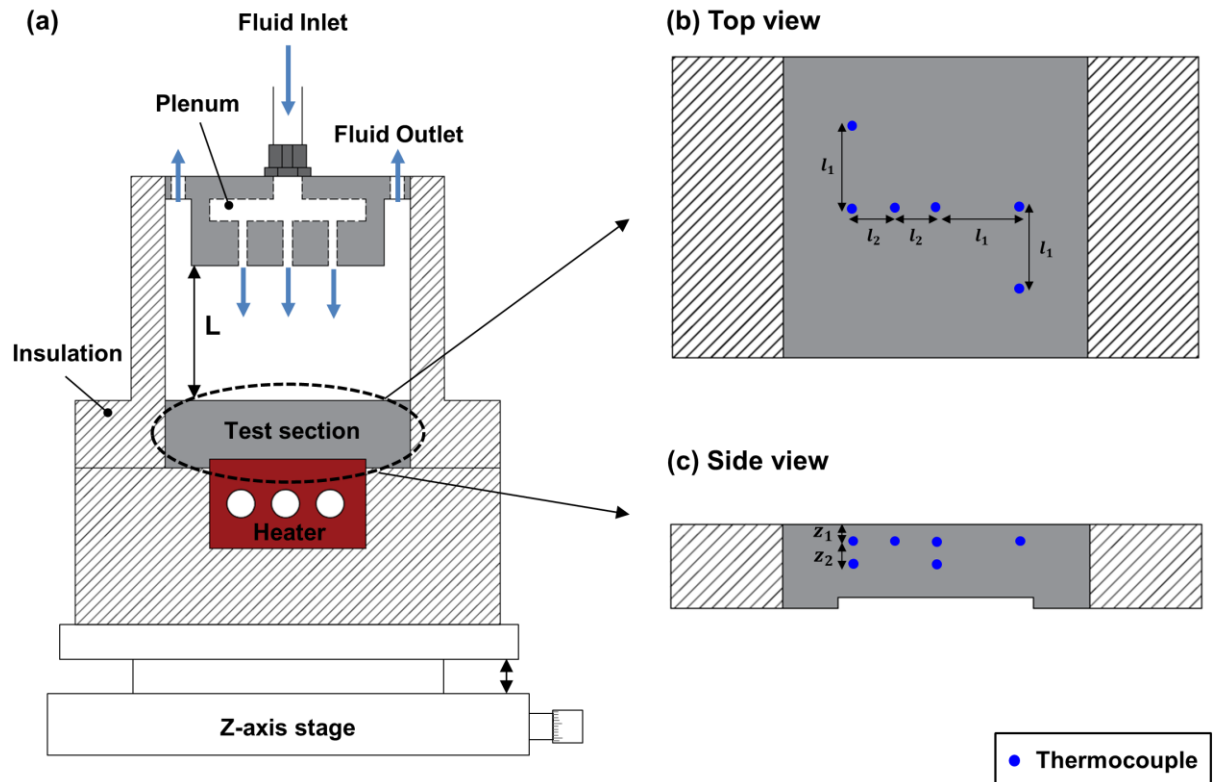


Fig. 4. Schematics of the (a) test module (b) top view of test section (c) side view of test section.

3.1.2. FDM process of 3D printing technique

3D printing is the additive manufacturing technique to fabricate the complex structures by successively adding filaments layer by layer, unlike conventional manufacturing method such as machining, casting, and forging. For the experiment which validation of numerical optimization results, the impinging jet arrays are manufactured by the 3D printing technique. Many researchers have been investigated the impinging jet with various method of fabrication techniques. Olesen et al. [39] presented the liquid jet cooling system by using plastic parts. Han et al. [40] studied the hybrid micro jet cooler which manufactured by silicone plate with etching process. Jörg et al. [41] investigated the reduction of thermal resistance via liquid jet cooling system which fabricated by micromachining. Natarajan et al. [42] were used the multilayer ceramic technology to build liquid jet cooling devices. These manufacturing techniques for jet impingement cooling system are expensive and difficult to create the complex geometries. Therefore, 3D printing technique is used to build complex geometries for impinging jet experiment in this study.

The Fused Deposition Modeling (FDM) technique for 3D printing is the most broadly used and works by using the filament. However, there is main issue that need to consider when manufacturing the structures by FDM process. The problem is that structures are undersized than CAD design modeling due to thermal contraction and expansion of the 3D printing material when it is heated and cooled. Thus, it is needed to develop the correlations between the 3D printed structure and CAD design modeling. Mazlan et al. [43] proposed the correlations of structures including, wire diameter, bridge, hole diameter, wall thickness, and overhang. Likewise, the correlations for the circular and elliptic horizontal hole printing are established in this study. As indicated in Eq. (3) and (4), it is confirmed that the correlations of circular and elliptic holes for the predicting contraction of PLA (Polylactic acid) are well fitted based on the coefficient of determination (R^2) which value 0.995 and 0.997 for circular hole and elliptic hole structures, respectively.

$$d_{measure} = 2.597d_{design}^3 - 11.625d_{design}^2 + 18.356d_{design} - 9.011 \quad (3)$$

(Circular hole, $R^2 = 0.995$)

$$a_{measure} = 4.549a_{design}^3 - 7.212a_{design}^2 + 4.601a_{design} - 0.611 \quad (4)$$

(Elliptic hole, $R^2 = 0.997$)

Fig. 5 depicts the schematic drawing of the FDM 3D printer. During the FDM process, the filament is feed to heater block by filament extruder. The filament is extruded and melted via heated nozzle, and then deposited on the heated bed in the foam of a semi-cylindrical. The detailed parameters and values for the 3D printing process are listed in Table 2. The heated bed ensures the

melted materials can be deposited stably, so bed temperature set as 70 °C. The layer thickness is 0.12 mm and infill density are 100%, which values ensure the 3D printed structures have a higher quality and strength to endure the high pressure. The printing speed is 50mm/s and it takes about 27 hours for 3D printing the impinging jet array.

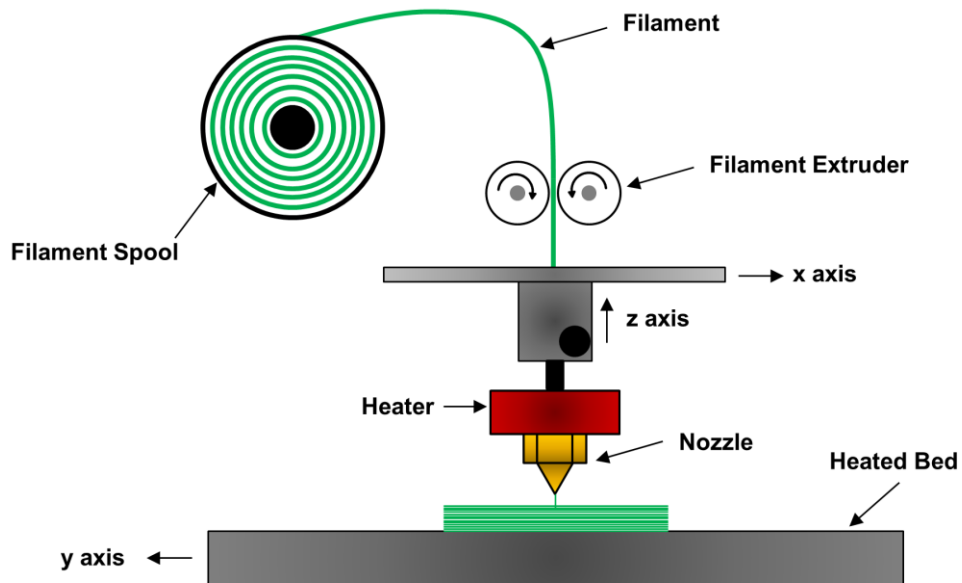


Fig. 5. Schematic of an FDM 3D printer.

Table 2. FDM process parameters and values for 3D printing.

Parameter	Value
Method	FDM (Fused Deposition Modeling)
Material	PLA (Polylactic acid)
Nozzle temperature	210 °C
Bed temperature	70 °C
Nozzle diameter	0.2 mm
Layer thickness	0.12 mm
Infill density	100 %
Printing speed	50 mm/s
Printing time	27 hours

3.1.3. Measurement procedure

In this study, the cooling performance is evaluated by comparing the stagnation heat transfer coefficient, stagnation temperature, and maximum temperature difference of target surface. Assumption that the heater and test section are completely insulated, 1-Dimensional thermal conduction equation is applied. The heat flux is evaluated by the Fourier's law based on the measured temperature, and then the surface temperature is calculated. In Eq. (5), the heat transfer coefficient is evaluated based on the reference value, nozzle inlet temperature.

$$h = \frac{q''}{T_s - T_{in}} \quad (5)$$

The error of T-type thermocouples is $\pm 0.5^\circ\text{C}$ or $\pm 0.4\%$ as the maximum value. The accuracy of the mass flow meter is $\pm 0.9\%$ in its full range, and power sources are $\pm 0.2\%$. The uncertainty of h is evaluated from the error propagation. The maximum uncertainty of h is about $\pm 7.88\%$, and the temperature difference is $\pm 0.707^\circ\text{C}$.

Fig. 6 shows the single impinging jet nozzle and 3D printed impinging jet array. The size of single nozzle hole is 2.0 mm. It is confirmed that the 3D printed array nozzle consisting of white color PLA is well matched the CAD design, as shown in Fig. 6(c) and (d). The 3×3 circular nozzle holes of diameter 1.5 mm are aligned in-line with an equal interval of jet-to-jet spacing (S) 10.5 mm. The 3D printed nozzle is fabricated with an infill ratio of 100% to ensure that working fluid is only ejected through the nozzle holes. As can be seen in Fig.7, the differences of average temperature between steel and 3D printed jet array are less than 0.4°C which value is less than uncertainty of T-type thermocouple. Therefore, it is confirmed that the results of impinging jet heat transfer using the 3D printed jet array is reliable. The initial circular impinging jet array (ICJ) is set as a reference configuration for the optimization study.

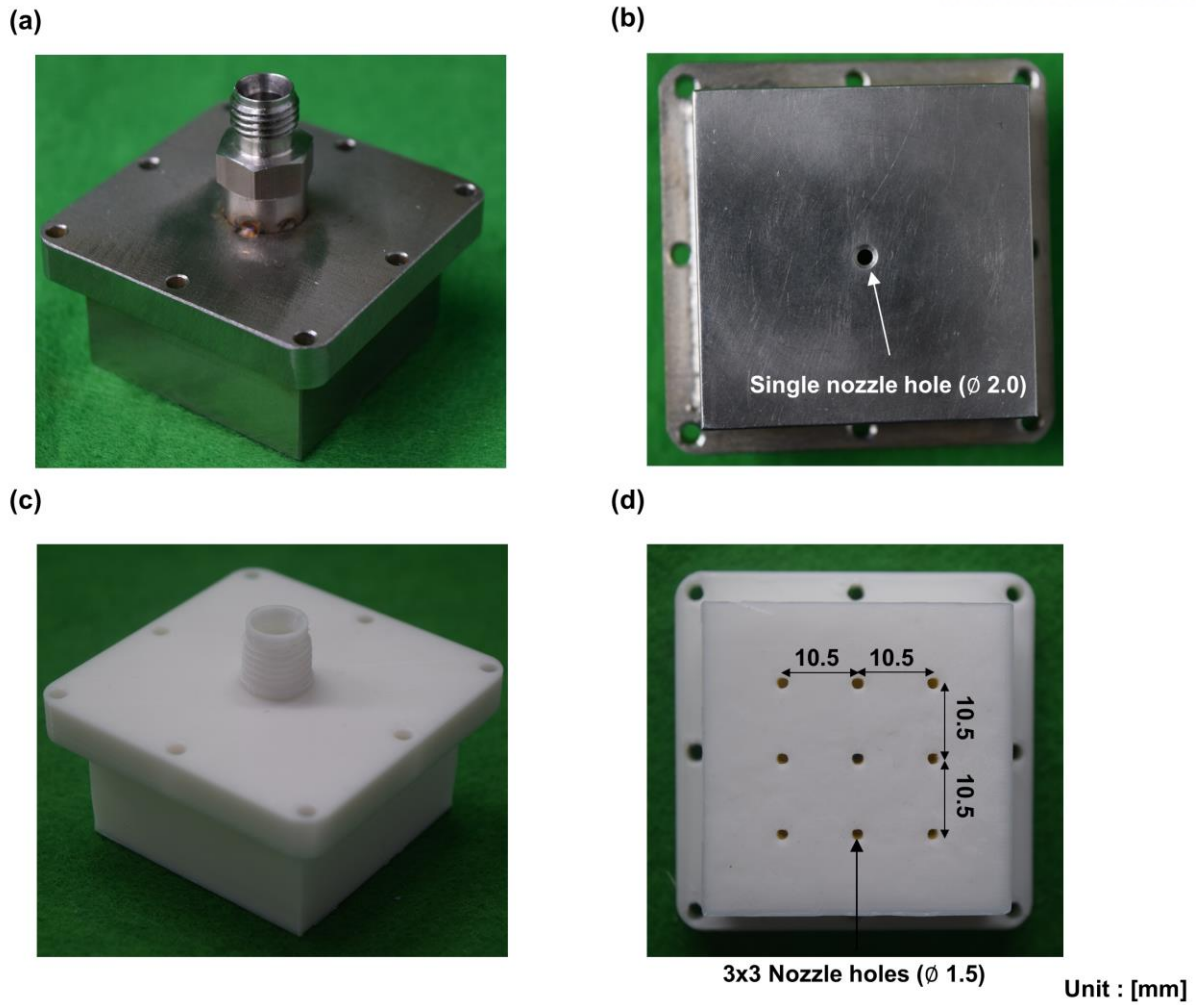


Fig. 6. Experimental model of impinging jet nozzle: (a, b) single impinging jet nozzle (c, d) 3D printed impinging jet array nozzle.

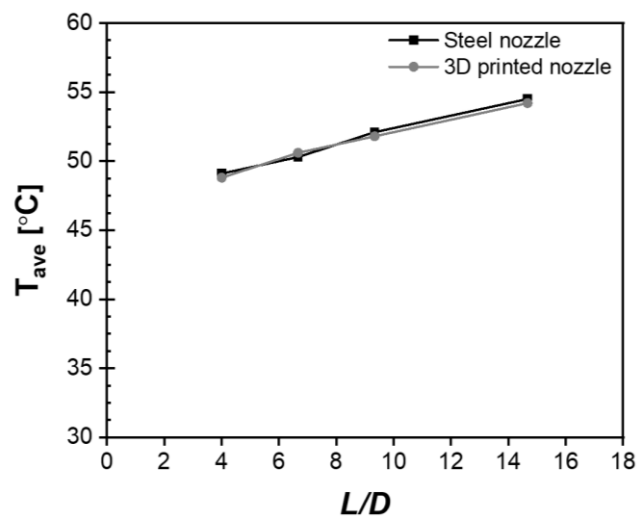


Fig. 7. Comparison of average temperature between steel and 3D printed jet array.

3.2. Results and discussion

The cooling characteristics of the single and array impinging jets with CO₂ and N₂ are evaluated. The nozzle-to-plate distances (L) are set as 1.0 to 14.6 nozzle diameter. The range of volume flow rates is 30.0 to 80.0 LPM. The jet Reynolds number is defined in Eq. (6) to normalize the experimental conditions.

$$Re_D = \frac{\rho V D}{\mu} \quad (6)$$

3.2.1. Effect of expansion

Fig. 8 depicts the temperature of nozzle inlet and outlet when without heating power to copper block. The temperature drops of CO₂ is about 3.49 °C and N₂ is about 0.64 °C under the value of NPR= 4.19 and NPR= 3.25, respectively. As mentioned earlier, the Joule-Thomson coefficient of CO₂ is four times higher than that of N₂, which means the temperature drop of CO₂ with a pressure drop is more dramatic than N₂. As Re_D increases, the effect of expansion increases due to a higher pressure drop ratio, so the flow has a lowered jet temperature.

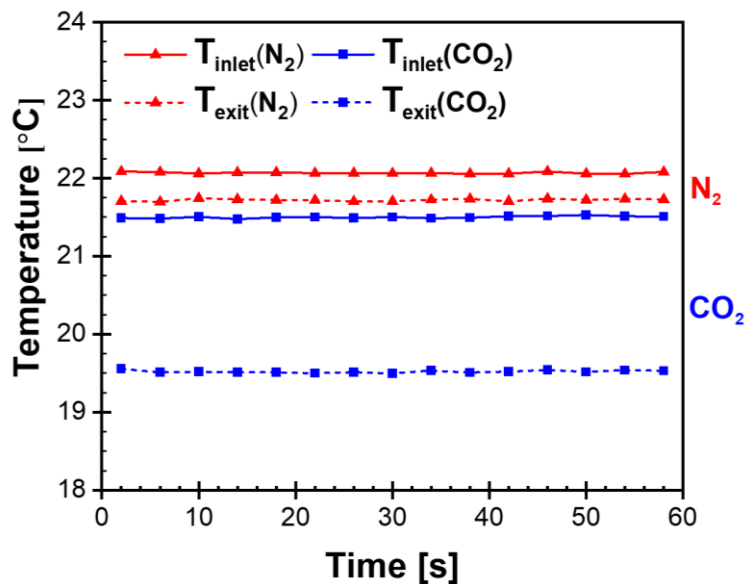


Fig. 8. Temperature drop of CO₂ and N₂ by expansion effect.

3.2.2. Effect of L/D

The cooling characteristics of single and array jets with various nozzle-to-plate distances (L/D) are investigated. In previous study, the heat transfer characteristics of the single impinging jet with varying L/D and Re_D was investigated by San et al. [44]. In general, at low L/D and high Reynolds number means that high momentum flows can impinge on the target plate, so leads to the enhanced heat transfer rates. In this experiment, this tendency is shown in the stagnation heat transfer coefficients, but slightly different for certain conditions of L/D and Re_D .

Fig. 9 shows stagnation heat transfer coefficients of single impinging jet. As L/D increases, the heat transfer coefficients are decreases, but there is a peak value of the heat transfer coefficient at the specific value of L/D . The value of L/D with maximum heat transfer coefficient tends to increase as the Re_D increases. In the case of $Re_D = 104,159$, the value of L/D with maximum heat transfer coefficient is 3.0 and when the Re_D is lower than 78,119 the peak value has at $L/D = 1.0$ or $L/D = 2.0$, as shown in Fig. 9 (a). The relations between heat transfer characteristics and vortices have been studied by Popiel and Fox et al. [45,46]. After the jet impinges the target surface, the jet flow grows to the wall jet region and jet vortices developed by confined wall and nozzle body. These vortices are beneficial to heat transfer enhancement and as Re_D increases, it means the more flow rate and lower temperature jet impinge the target plate. Fig. 9(b) illustrates the trend of heat transfer coefficients of N_2 impinging jet with varying L/D , but the maximum value of heat transfer coefficient is not shown clearly. As previously discussed, the temperature drops of N_2 is less sensitive than CO_2 by pressure drop, thus resulting in the peak value are not clearly distinguished at high a Re_D .

Fig. 10 shows the heat transfer coefficient with varying L/D for array impinging jets by using CO_2 and N_2 jet. Compared to the single impinging jet, the stagnation heat transfer coefficient of array impinging jets linearly decreases as L/D increases. As Re_D increases, the stagnation heat transfer coefficient is increases. At the high Re_D , the heat transfer coefficients are more increases rapidly than low Re_D . As can be seen Fig. 10(a) and (b), the heat transfer coefficients of N_2 are less sensitive with varying of L/D . These results are considered to be due to the difference of Joule-Thomson coefficient between CO_2 and N_2 .

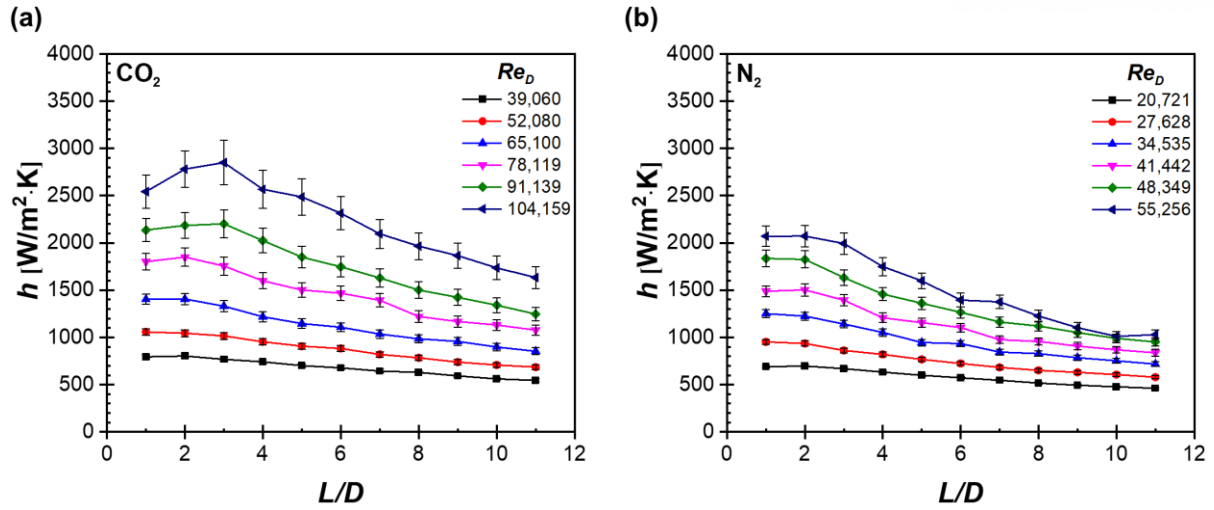


Fig. 9. Stagnation heat transfer coefficient distributions: (a) single CO_2 impinging jet (b) single N_2 impinging jet.

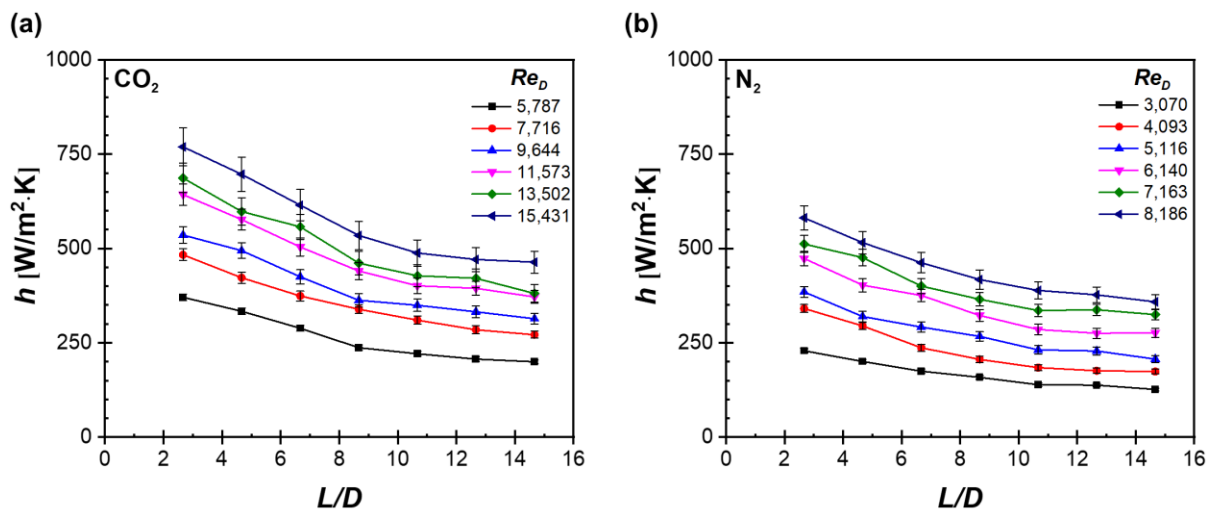


Fig. 10. Stagnation heat transfer coefficient distributions: (a) array CO_2 impinging jet (b) array N_2 impinging jet.

3.2.3. Effect of Re_D

Fig. 11 depicts the stagnation heat transfer characteristics of single CO_2 and N_2 impinging jet with varying Re_D at $L/D=2.0, 4.0, 8.0,$ and 10.0 . As Reynolds number increases, the larger flow rates and higher nozzle inlet pressures are guaranteed, so the low-temperature jets can be ejected from the nozzle. Therefore, the high Re_D enhances the heat transfer coefficient, both cases of CO_2 and N_2 impinging jet. As mentioned above, the small L/D ensures that jets with high momentum impinge the target plate, resulting in a high heat transfer rate. Compared to Fig. 11(a) and (b), the heat transfer coefficient of single CO_2 impinging jet is more sensitive to Re_D increasing than N_2 .

Fig. 12 shows the heat transfer coefficient of array CO_2 and N_2 impinging jet with varying Re_D with the value of $L/D=2.67, 4.67, 8.67,$ and 12.67 . Like the single impinging jet, the high Re_D and low L/D guarantee the enhanced heat transfer coefficient. The heat transfer coefficient of array impinging jet increases more rapidly at the high Re_D than low Re_D . These result shows that the high Re_D yield the jet-to-jet interaction to beneficial the heat transfer improvement. Compared to array CO_2 and N_2 impinging jet, the heat transfer coefficients of CO_2 jet are more sensitive to the value of L/D than N_2 jet as shown Fig. 12(a) and (b). These results are due to that the lowered temperature of CO_2 jet by the Joule-Thomson effect at low L/D condition.

Fig. 13 shows a comparison of the stagnation heat transfer coefficient between single and array impinging jet with various Re_D and volume flow rate at $L/D=2.0$. For the condition of the same Re_D , the stagnation heat transfer coefficient of N_2 impinging jet is higher than that of CO_2 impinging jet as shown in Fig. 13(a) and (b). The heat transfer coefficient of single N_2 impinging jet from $Re_D=55,256$ is nearly twice higher that of single CO_2 impinging jet from $Re_D=52,079$. However, as shown in Fig. 13(c), if the reference value of the flow rate is chosen as the volume flow rate, CO_2 jet has a higher heat transfer coefficient than N_2 jet under all conditions. This phenomenon is due to the difference in the thermal properties that affect the Re_D , such as the viscosity of the CO_2 and N_2 . As the volume flow rate increases, the pressure drops of the gas ejected from the nozzle increases and the difference of the heat transfer coefficient increases because CO_2 has a higher Joule-Thompson coefficient than N_2 . The stagnation heat transfer coefficient of the single impinging jet is always higher than that of the array impinging jet due to concentrated flow rates to the stagnation point.

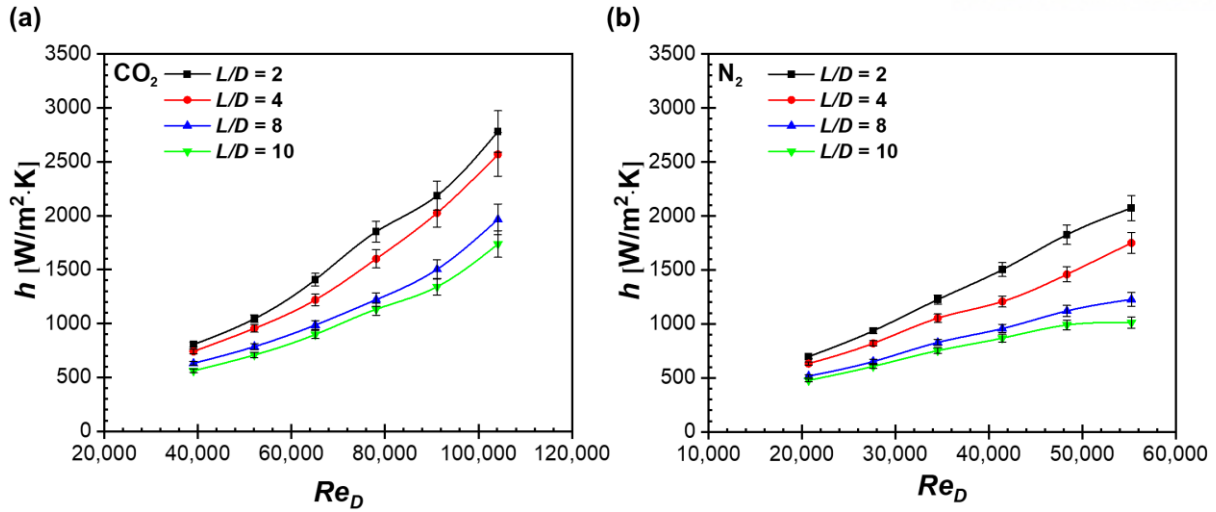


Fig. 11. Stagnation heat transfer coefficients varying with Reynolds number: (a) single CO_2 impinging jet (b) single N_2 impinging jet.

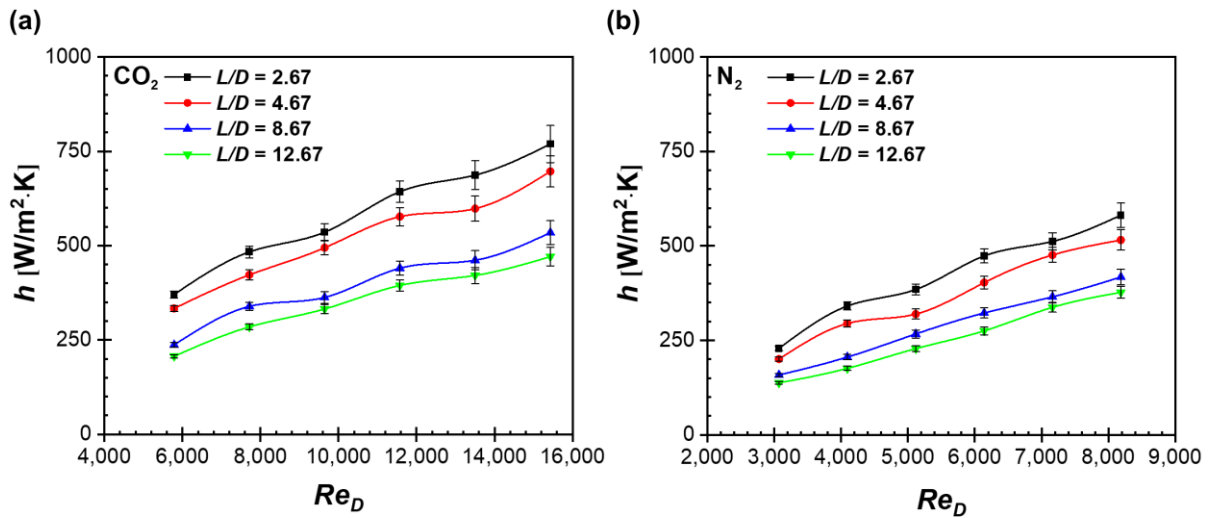


Fig. 12. Stagnation heat transfer coefficients varying with Reynolds number: (a) array CO_2 impinging jet (b) array N_2 impinging jet.

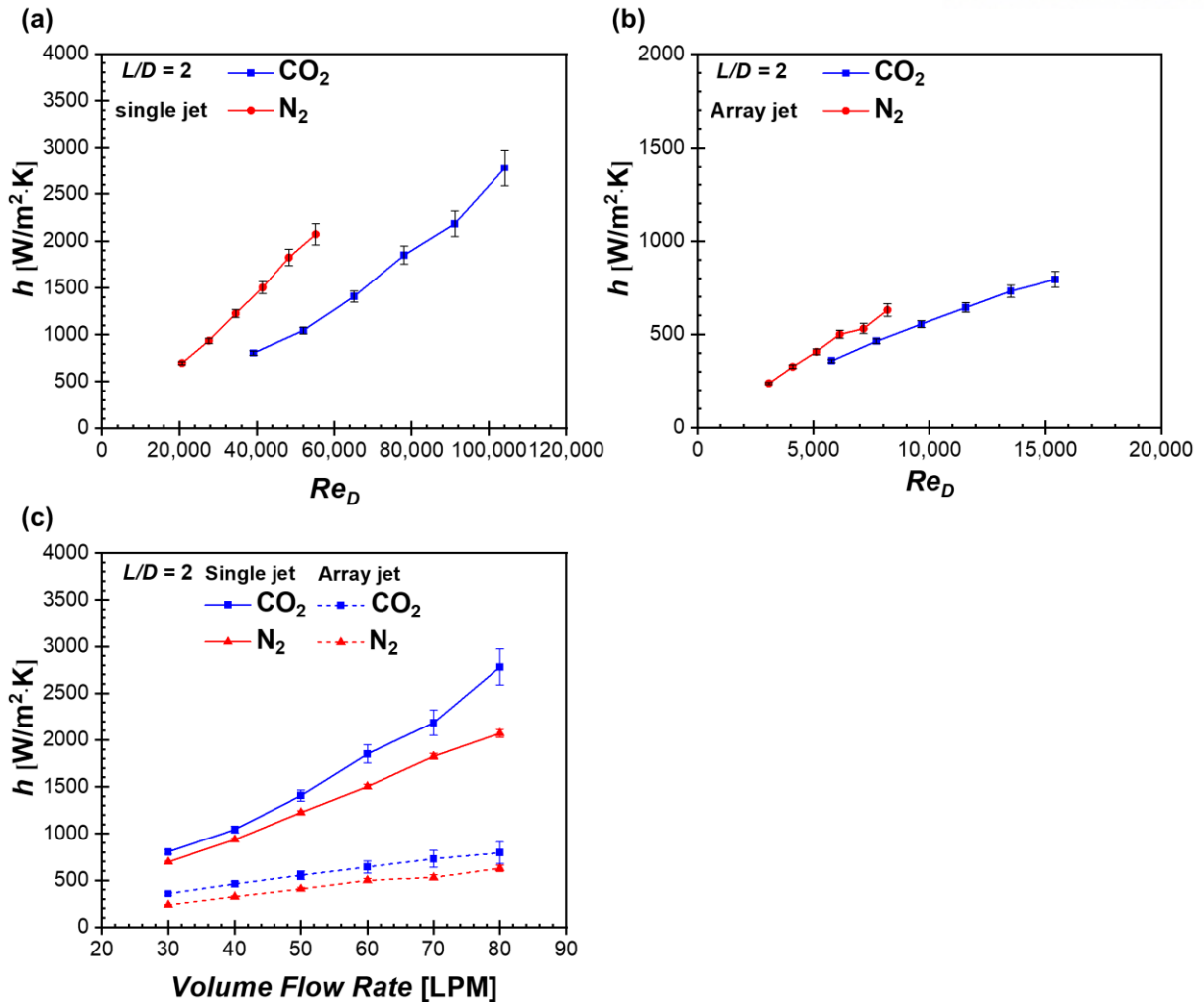


Fig. 13. Stagnation heat transfer coefficients varying with Reynolds number at fixed $L/d=2$: (a) single impinging jet (b) array impinging jet (c) effect of working fluid with varying volume flow rate.

3.2.4. Temperature non-uniformity

For the evaluation of the cooling performance of temperature uniformity, the maximum temperature difference (T_{dif}) of six thermocouples is chosen as the indication of the temperature non-uniformity, which is defined in Eq. (7). As the value of temperature non-uniformity is higher, the cooling uniformity of the target surface is deteriorated.

$$T_{dif} = T_{max} - T_{min} \quad (7)$$

Fig. 14 shows comparison of temperature non-uniformity and average temperature of test section between single and array impinging jet with varying volume flow rate at $L/D=2.0$. As shown in Fig. 14(a), array jet has a higher performance of cooling uniformity than that of single impinging jet under all volume flow rate condition. Fig.14 (b) shows a comparison of array impinging jet between CO_2 and N_2 with varying volume flow rate. The average temperature is the mean temperature of the eight thermocouples inserted into the test section. Under all volume flow rate conditions, the temperature non-uniformity of the test section by the array impinging jet cooling is little different, which means that it has a similar level of cooling uniformity. However, there is a big difference in the average temperature of the test section and the largest temperature difference is about $8.45\text{ }^\circ\text{C}$. Therefore, the array impinging jet has a more uniform cooling performance than a single impingement jet, and the array CO_2 impinging jet guarantees a lower surface temperature than the array N_2 impinging jet.

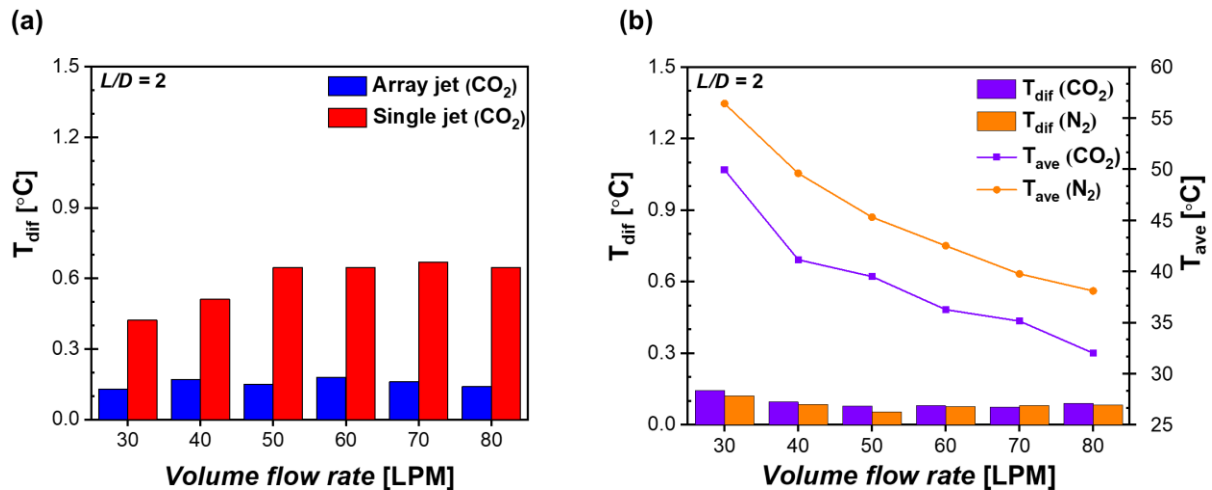


Fig. 14. Comparative plots showing the temperature non-uniformity of (a) single and array impinging jet (b) array impinging jet with CO_2 and N_2 .

4. Part II: Geometry optimization and confirmation experiments

4.1. Computational details

4.1.1. Governing equations

The numerical modeling for the optimization study is performed by the commercial CFD codes, ANSYS Fluent 19.0. ANSYS Fluent uses the cell-centered finite volume method (FVM) to discretize and solve the governing equations based on Reynolds averaged Navier-Stokes (RANS) approach. The working fluid (CO_2) is set as real gas and state of the flow is steady and fully turbulent. The second-order upwind scheme is used to discretize the diffusive term. The pressure-velocity coupling is achieved by a coupled algorithm, which has been proved a robust and efficient scheme. The coupled algorithm solves the momentum and pressure-based continuity equation together, so it has a superior performance compared to the segregated solution algorithm. In the simulation, the iteration of solutions is continued until the convergence criterion which set as the normalized residuals of mass, momentum, and energy equations decrease below the 10^{-4} , 10^{-4} , and 10^{-9} at each iteration, respectively. Also, the average temperature of the impinging surface is monitored, and the solutions are considered to be converged when the monitored value was not changed within the 100 iterations. The governing equations are as follows:

Continuity:

$$\frac{\partial(\rho U_i)}{\partial x_i} = 0 \quad (8)$$

Momentum:

$$\frac{\partial(\rho U_i U_j)}{\partial x_j} = -\frac{\partial P}{\partial x_i} + \mu \frac{\partial}{\partial x_j} \left(\frac{\partial U_i}{\partial x_j} + \frac{\partial U_j}{\partial x_i} \right) + \frac{\partial}{\partial x_j} (-\rho \overline{u_i' u_j'}) \quad (9)$$

Energy:

$$C_p \frac{\partial(\rho U_i T)}{\partial x_i} = \frac{\partial}{\partial x_i} \left(\lambda \frac{\partial T}{\partial x_i} - \rho C_p \overline{u_i' T'} \right) \quad (10)$$

Where U, T, P are the time-averaged velocity, temperature, and pressure of the fluid. u' and T' are the velocity and temperature fluctuation. $\overline{u_i' T'}$ and $\overline{u_i' u_j'}$ are the turbulence heat flux vector and Reynolds stress term which based on the Boussinesq assumption and these values are defined as:

$$-\overline{u_i' u_j'} = \mu_t \left(\frac{\partial U_i}{\partial x_j} + \frac{\partial U_j}{\partial x_i} \right) - \frac{2}{3} \left(\rho k + \mu_t \frac{\partial U_i}{\partial x_i} \right) \delta_{ij} \quad (11)$$

$$-\rho \overline{u_i' T'} = \frac{\mu_t}{Pr_t} \left(\frac{\partial U_i}{\partial x_i} \right) \quad (12)$$

Where $\mu_t = \rho C_\mu (k^2/\varepsilon)$ is the turbulent viscosity, δ_{ij} is the Kronecker delta.

4.1.2. Turbulence and near-wall modeling

The flow region of the impinging jet lies in the fully turbulent flow, so the realizable k- ε turbulence model is adapted in this study. The standard k- ε turbulence model was proposed by Launder and Spalding [47]. This model involves the transport equations for turbulent flow such as the turbulence kinetic energy (k) and the rate of dissipation (ε). Compared to the standard k- ε turbulence model, the realizable k- ε turbulence model contains an alternative equation for the eddy viscosity and a modified transport equation for the dissipation rate. As a result, the realizable k- ε turbulence model accurately predicts the jet spreading and near-wall turbulence effects than the standard k- ε turbulence model [48-50]. The detailed transport equations as follows:

$$\frac{\partial(\rho k u_j)}{\partial x_j} = \frac{\partial}{\partial x_j} \left[\left(\mu + \frac{\mu_t}{\sigma_k} \right) \frac{\partial k}{\partial x_j} \right] + G_k + G_b - \rho \varepsilon - Y_m + S_k \quad (13)$$

$$\frac{\partial(\rho \varepsilon u_j)}{\partial x_j} = \frac{\partial}{\partial x_j} \left[\left(\mu + \frac{\mu_t}{\sigma_\varepsilon} \right) \frac{\partial \varepsilon}{\partial x_j} \right] + \rho C_1 S_\varepsilon - \rho C_2 \frac{\varepsilon^2}{k + \sqrt{\nu \varepsilon}} + C_{1\varepsilon} \frac{\varepsilon}{k} C_{3\varepsilon} G_b + S_\varepsilon \quad (14)$$

Where G_k and G_b are referred to the production of turbulence kinetic energy due to the mean velocity gradients and buoyancy. S_k and S_ε are the user-defined source terms. σ_k and σ_ε are referred to the turbulent Prandtl numbers based on k and ε , respectively. C_1 , C_2 , $C_{1\varepsilon}$, and $C_{3\varepsilon}$ are the empirical constants. Y_m represents the contribution of the fluctuating dilatation.

One of the most important considerations to the numerical study of jet impingement heat transfer is in the vicinity of the impinging surface, especially the near-wall viscosity affected layer. The enhanced wall treatment (EWT) is a two-layer methodology for wall treatments and used to evaluate the eddy viscosity in the near-wall. In EWT model, the whole domain is subdivided into a viscosity affected region ($Re_y < 200$) and fully turbulent region ($Re_y > 200$) depending on turbulent Reynolds number (Re_y). Therefore, the more accurate results near-wall region can obtain by applying the EWT. The turbulent Reynolds number (Re_y) defined as:

$$Re_y = \frac{\rho y \sqrt{k}}{\mu} \quad (15)$$

Where y denotes the wall-normal distance calculated at the cell centers. For the viscosity affected region, the one equation of Wolfstein [51], the turbulent eddy viscosity and dissipation are evaluated by algebraic expressions. For the fully turbulent region, the realizable k- ε turbulence model is employed. In EWT for momentum and energy equations, the law of the wall formulated to extend its applicability throughout the near-wall region by blending the linear (laminar) and logarithmic (turbulent) using a

function suggested by Kander [52]. The temperature and velocity of the near-wall region are obtained by blending the laminar linear sublayer and turbulence logarithmic laws. The blended law of the wall function as follows:

$$u^+ = e^{\Gamma} u^+_{laminar} + e^{1/\Gamma} u^+_{turbulent} \quad (16)$$

$$\Gamma = -\frac{\alpha(y^+)^4}{1 + \beta y^+} \quad (17)$$

$$T^+ = e^{\Pi} T^+_{laminar} + e^{1/\Pi} T^+_{turbulent} \quad (18)$$

$$\Pi = -\frac{\alpha(y^+ Pr)^4}{1 + \beta Pr^3 y^+} \quad (19)$$

Where $y^+ = y_p u_\tau / \nu$ is the dimensionless height of the first layer cells near the wall, y_p is the actual height of the first layer cell, u^+ is the dimensionless velocity which defined as velocity over the shear velocity, τ_w is the wall shear stress, and u_τ is the shear velocity. Γ and Π are blending functions, and the value of constants is specified as $\alpha = 0.01$ and $\beta = 5$.

4.1.3. Computational domain and boundary conditions

The schematic drawings of the computational domain and boundary conditions for the array impinging jet cooling simulation are shown in Fig. 15. The inlet boundary condition is set as the temperature 294 K and velocity 15.78 m/s, which is equivalent to the value of volume flow rate $5 \times 10^{-4} \text{ m}^3/\text{s}$ and outlet is set as pressure outlet boundary condition. The nozzle-to-plate distance (L), nozzle diameter (d), and jet-to-jet spacing (S) are set as 4.0 mm, 1.5 mm, and 10.5 mm, respectively. The bottom of solid domain is set as constant heat flux condition. Fig. 15(c) illustrates the CAD rendering image of impinging jet array. The structure of the outlet is replaced as the square based on the same hydrodynamic diameter to ease of grid generation. The nine nozzle holes (3×3) are arranged at equal intervals on the impinging jet array. For the purpose of reducing the computational cost, the entire domain is simplified to the one-quarter domain by applying the symmetry plane. Although the numerical simulations are performed for a small part of the domain, symmetry planes facilitated the computation which considering the 3×3 array nozzle holes. The adiabatic and no-slip boundary conditions are applied to walls except for the impinging surface.

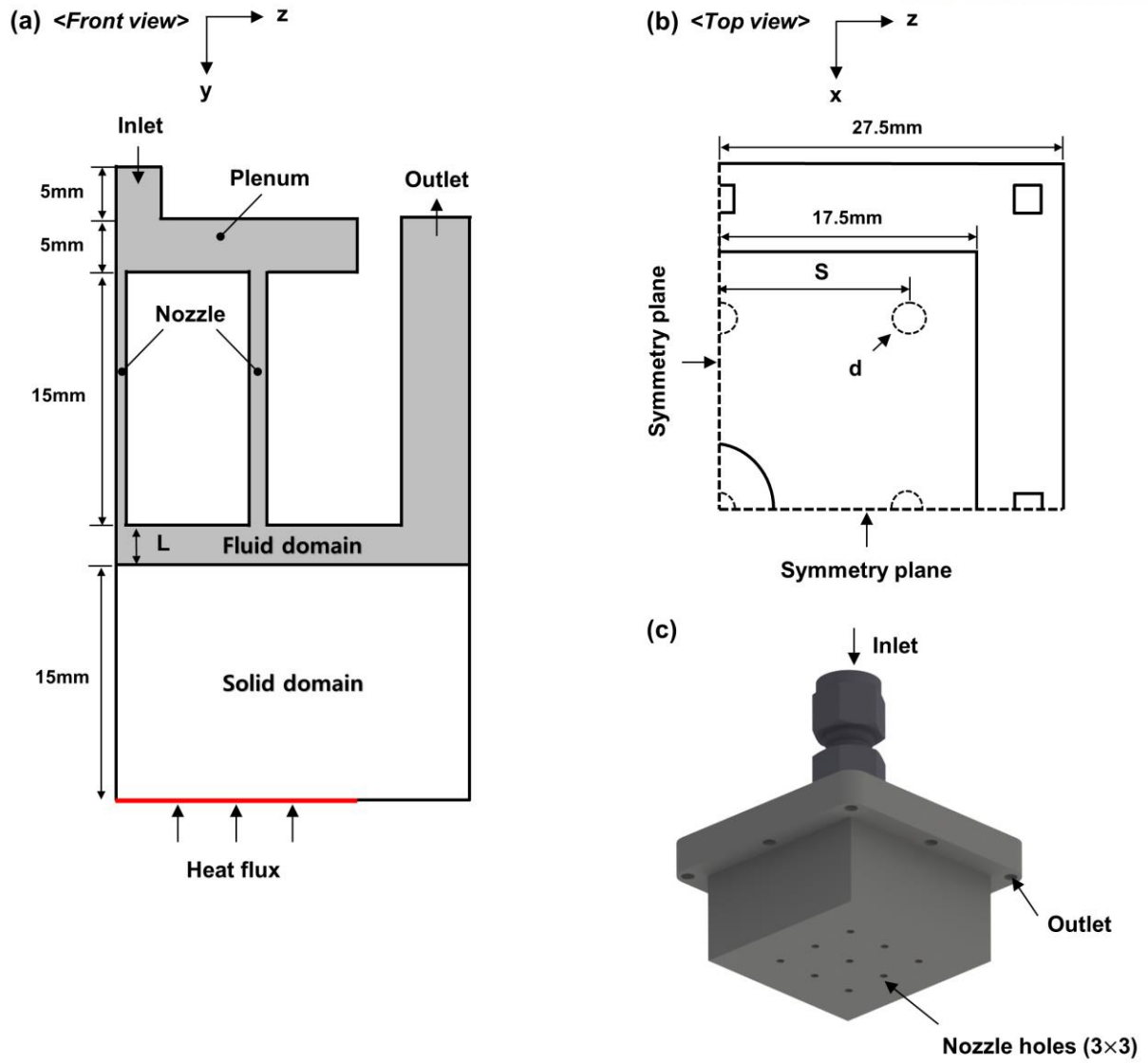


Fig. 15. Schematics of the computational domain and boundary conditions: (a) front view (b) top view (c) CAD rendering image of impinging jet array.

4.1.4. Grid independence test

The computational domain is generated as a hexahedral grid system with refined meshing near the walls by using ANSYS meshing, as shown in Fig. 16. Due to the enormous gradients of temperature and thermo-physical properties near the impinging wall, much finer grids are required in the vicinity of the impingement surface to resolve the near-wall region with EWT. To ensure the accurate predictions of the near-wall region, the dimensionless distance from the wall (y^+) is kept less than unity in this study. To check the grid independency on the numerical results, four different grid numbers are used in the calculation. Fig. 17 shows the local temperature distributions depending on the grid numbers. The maximum differences between the used and fine grid are within the 0.1 K, so the grid number 2.78×10^6 , which ensures the grid-independent results, is used in this study.

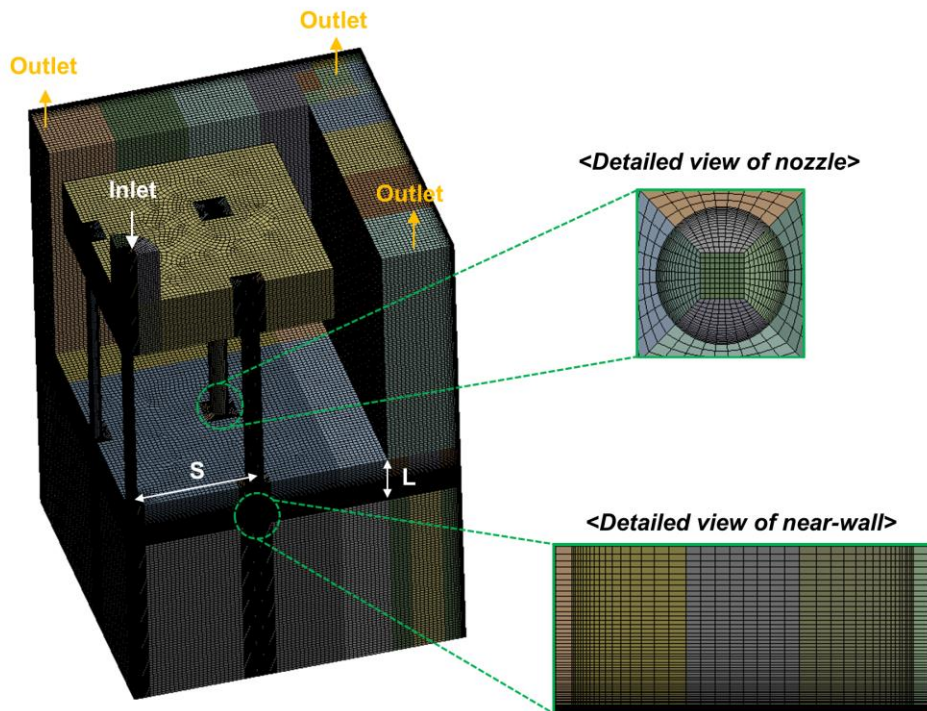


Fig. 16. The computational domain and grid system.

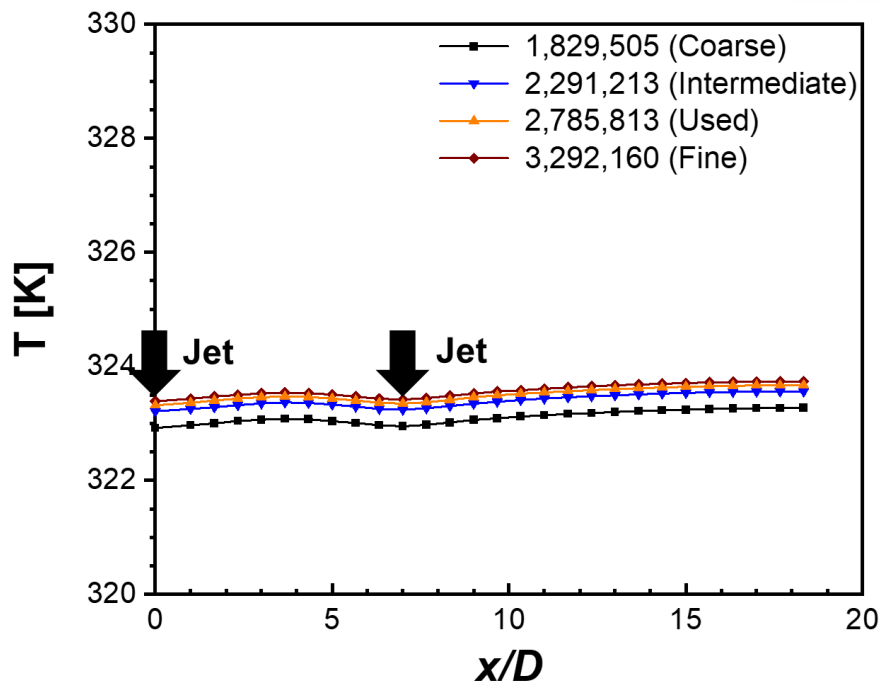


Fig. 17. The grid independence test.

4.2. Optimization strategy

First of all, the fixed and design parameters should be determined in order to optimization study. The fixed parameters are the nozzle arrangement and number of nozzles. Due to the previous study revealed that the inline arrangement has outperformed the staggered arrangement [18], so the nozzle arrangement is selected as the inline and radial is selected as a comparison arrangement. The design parameters are selected except those that can be changed by experimental method, such as Re_D and L/D . The jet-to-jet spacing, and nozzle size is the major parameters for affecting the temperature uniformity and local temperature distributions, respectively [17,56]. For array impinging jet, it is important to consider the effects of nozzle size at the central and outer of jet array due to the non-uniform distribution of mass flow rate. Therefore, jet-to-jet spacing (S), diameter of central nozzle (d_c), diameter of outer nozzle (d_o), minor axis length (a), and aspect ratio ($AR = b/a$) are selected as the design parameters, as can be seen in Fig. 18.

The geometry of nozzles is selected as the circular and elliptic nozzles based on the prior studies. The conventional circular jet has outperformed the triangle and rectangular jet, but elliptic jet with specific aspect ratio has outperformed the circular jet and yield the uniform heat flux of target surface [57,58]. Unlike the circular jets that grow in axisymmetric, the elliptic jets produce the azimuthal curvature variation which evolves in different ways [24]. Therefore, the flow patterns and cooling characteristics of array elliptic and circular jets will be different. Namely, the enhanced cooling performance can be expected through the stronger jet-to-jet interactions by placing the circular nozzle and elliptic nozzle at the central and outer of the jet array, respectively. The circular nozzle arranged inline and radial are named CJ1 and CJ2. Also, the jet array consisting of the outer elliptic nozzle arranged in a different direction and central circular nozzle are named EJ1 and EJ2, respectively. The objectives of optimization study and range of design parameters are shown below:

Multi-Objective:

$$\text{Minimize - } T_{ave} (S, d_c, d_o, a, AR)$$

$$\text{Minimize - } T_{dif} (S, d_c, d_o, a, AR)$$

Subject to:

$$6.0 \text{ mm} \leq S \leq 15.0 \text{ mm}, 1.0 \text{ mm} \leq d_c \leq 2.0 \text{ mm},$$

$$1.0 \text{ mm} \leq d_o \leq 2.0 \text{ mm}, 0.4082 \text{ mm} \leq a \leq 0.8165 \text{ mm},$$

$$1.5 \leq AR \leq 3.0$$

The optimization study aims to find the optimal geometry of jet array that satisfies the objective function which minimize the average temperature (T_{ave}) and maximum temperature difference (T_{dif}) of the target surface. The range of geometric parameters about the nozzle size such as d_c , d_o , a , and AR are selected based on the same area.

The optimization process is divided into three steps, design of experiment (DoE), response surface methodology (RSM), and optimization. Fig. 19 shows the overall flow chart of the optimization procedure. Firstly, 29 DoE points are generated using the central composite design (CCD) method. The CCD method was established by Box and Wilson [53] and widely used in due to its performance of ideal solution for a second-order response surface fitting by selecting corner, axial and center points. Also, the RSM is used in various applications due to its merit that easy to numerically by approximating a complex design space using average values and deviations.

The response surfaces are build based on the CFD simulation results of DoE points using the Kriging model. The Kriging model is an interpolating technique and has several advantages over other interpolation methods. Firstly, the Kriging model simulates an unknown point using information from some estimated points. In addition, the Kriging model can analyze both global and local statistical properties [54]. As such, the Kriging model is suitable for CFD calculation which has a high strength of non-linearity. If the quality of the response surface is poor, the optimization process returns to the first step and adds the number of DoE points and then builds the response surface again until the quality meets the criteria. The final step is the optimization of design parameters using the multi-objective genetic algorithm (MOGA). The MOGA is the modification algorithm of genetic algorithm (GA) which based on the law of survival of fittest in order to find the multiple non-dominated solutions in a single run [55]. The MOGA based on the non-dominated sorted genetic algorithm-II (NSGA-II) that uses the elitism concept to find the Pareto-front, which is classified as non-dominated solutions. In order to verify the candidate for optimization result, the CFD calculation (real solve) is performed. If the difference between the CFD calculation and the candidate of optimization result is less than 5 %, select the candidate to optimal solution and return to the first step, DoE, if exceed than 5 %.

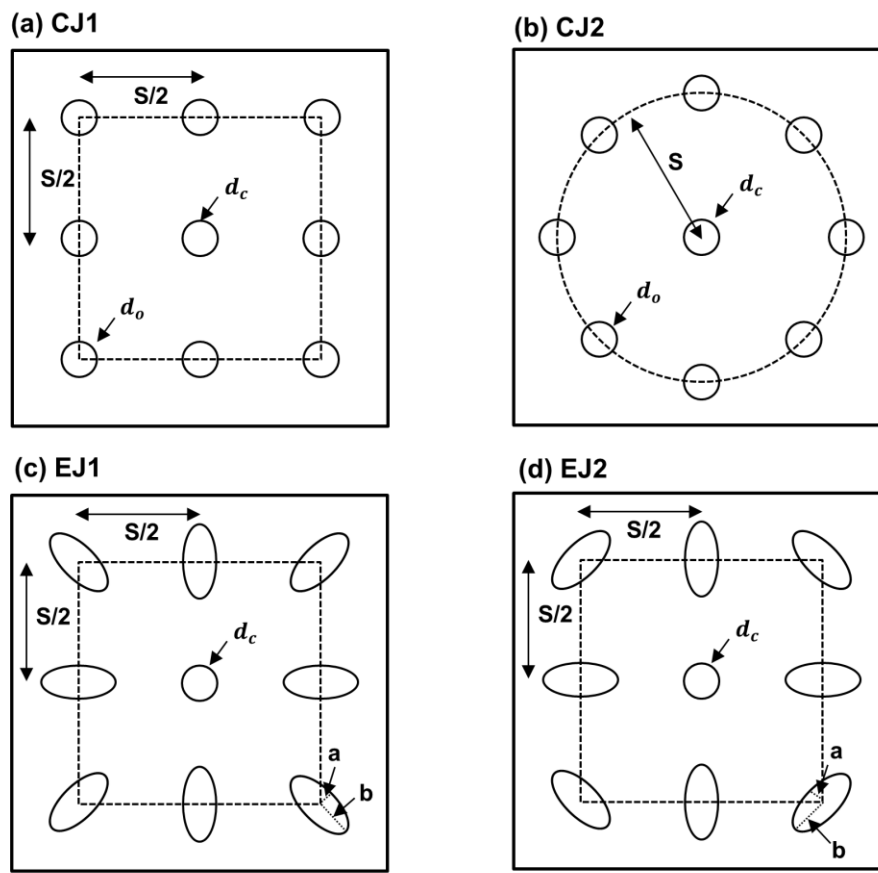


Fig. 18. Schematics of design parameters: (a, b) circular nozzle arranged inline and (c, d) radial outer elliptic nozzle arranged in a different direction.

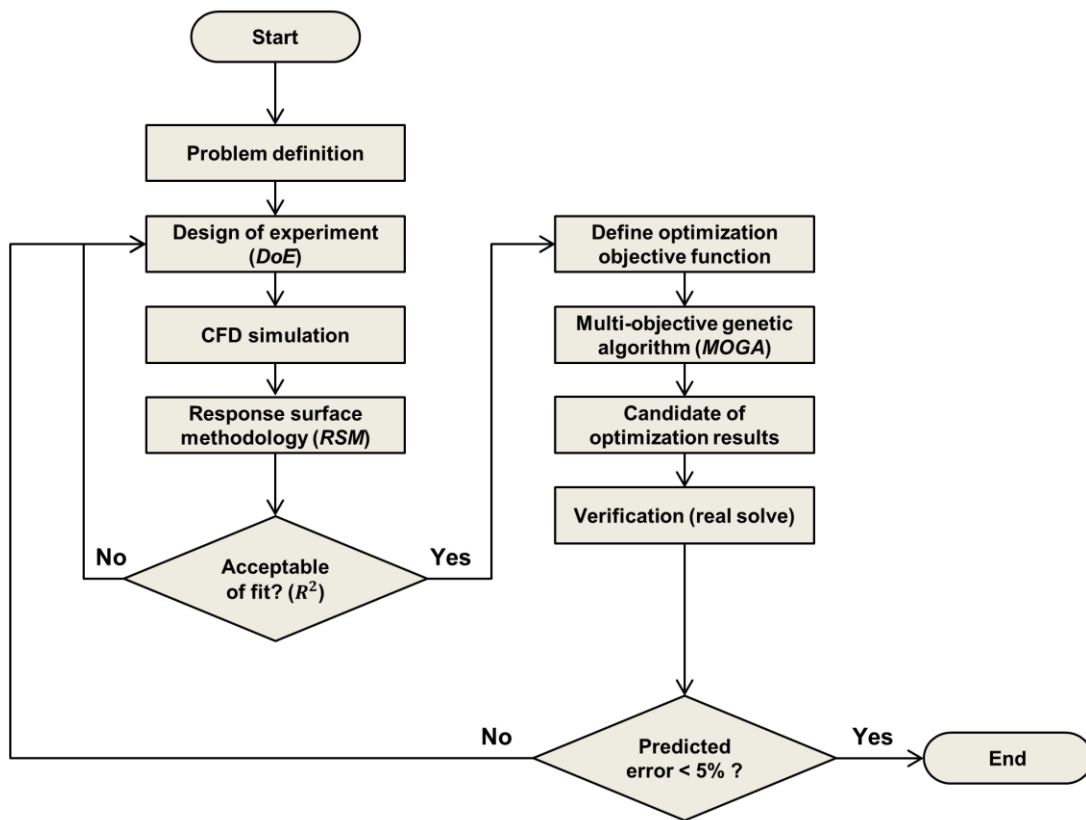


Fig. 19. The flow chart of the optimization procedure.

4.3. Results and discussion

4.3.1. Optimization results

In general, there are no solutions to optimize all objective functions simultaneously in multi-objective optimization problems. One of the promising ways to solve these problems requires the sacrifice of other objective functions to improve some objective functions, and in the same way, the MOGA approach finds the optimal solutions that are not dominated by the other optimal candidates through NSGA-II. The non-dominated solutions are called the Pareto optimal solutions, and the set of non-dominated optimal solutions is called the Pareto-front. Fig. 20 shows the trade-off chart in the optimization process. The best set of optimal solutions is the blue, and gradually turn to red as the solutions became deteriorate. The objective functions of this study are the minimize the average temperature (T_{ave}) and maximum temperature difference (T_{dif}) of the target surface. Therefore, the optimal design can be obtained near the left bottom corner in the coordinate system. Among the Pareto-front, the candidate of optimum design is sorted by the decision support process (DSP) which based on the direct Monte Carlo method. The DSP takes into account the weighted objective functions and ranks the candidate points using a uniform distribution. The weighted functions of the objective are set as default, which means that the importance of the output parameters is identical. Table 3 shows the best designs among the candidates selected by the MOGA approach for the CJ1, CJ2, EJ1, and EJ2, respectively. To verify the optimization results, the real solve (CFD calculation) is performed to examine them and the predicted error between optimization result and CFD simulation is less than 5 % in all cases. It is observed that the nozzle diameter at the outer of jet array (d_o) is slightly larger than nozzle diameter at the central of jet array (d_c) due to it can be cover the larger cooling area. Compared with the initial design, it is observed that in the case of EJ2, the T_{ave} and T_{dif} (temperature non-uniformity) is improved by about 7.6 K and 7.7 %. Among the optimum designs, the elliptic jet array has outclassed of cooling performance the circular jet array, the best case is the EJ2 and the worst case is the CJ2.

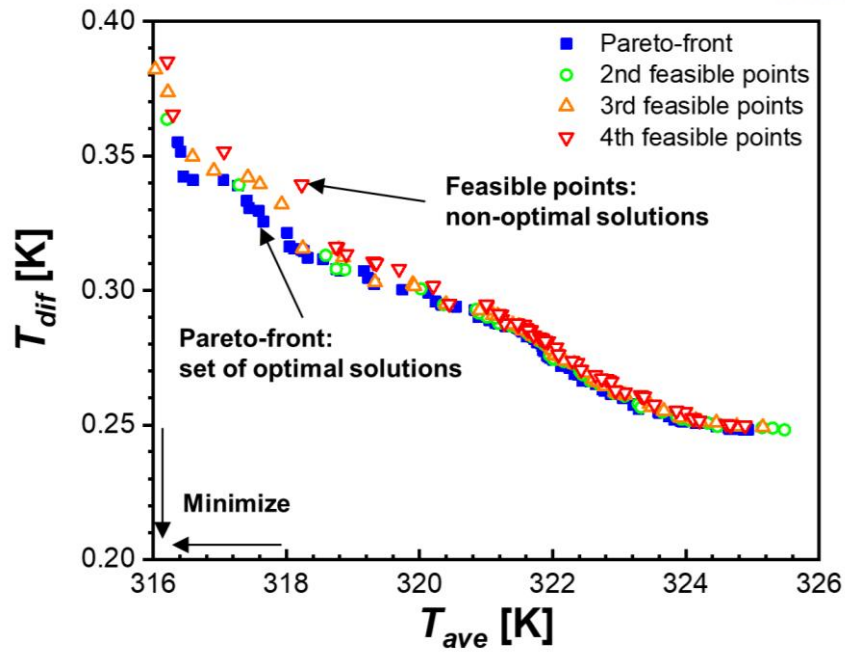


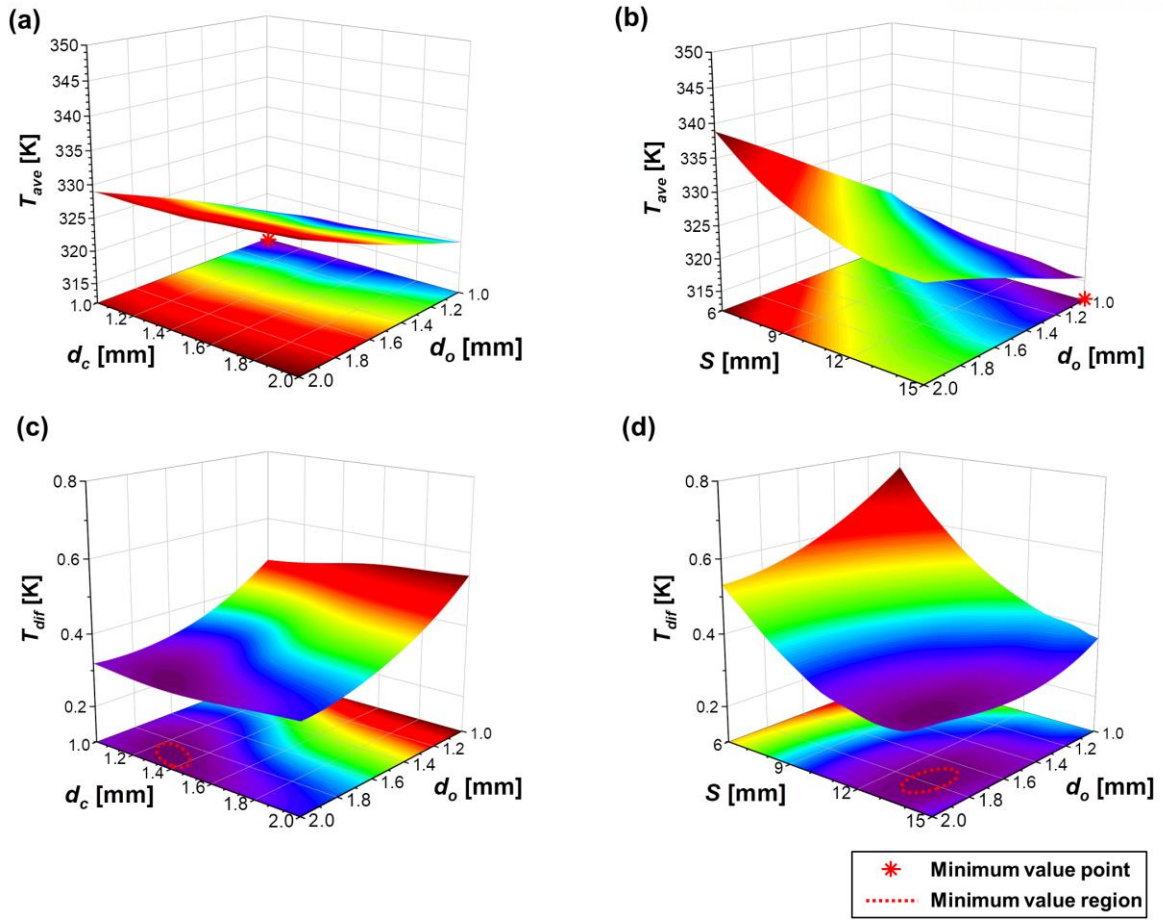
Fig. 20. The trade-off chart in the optimization process.

Table 3. The optimization results based on MOGA approach.

	S [mm]	d_c [mm]	d_o [mm]	a [mm]	AR [-]	T_{ave} [K]	T_{dif} [K]
Initial design	10.5	1.5	1.5	-	-	323.47	0.366
Optimum design (CJ1)	14.6	1.0	1.1	-	-	316.6	0.341
Verification						316.96	0.345
(Predicted error)						(0.1%)	(1.1%)
Optimum design (CJ2)	15.0	1.1	1.1	-	-	316.9	0.344
Verification						317.9	0.361
(Predicted error)						(0.3%)	(4.9%)
Optimum design (EJ1)	13.8	1.0	-	0.42	1.55	315.8	0.346
Verification						316.5	0.332
(Predicted error)						(0.2%)	(4.0%)
Optimum design (EJ2)	14.7	1.0	-	0.41	1.55	316.1	0.351
Verification						315.9	0.338
(Predicted error)						(0.06%)	(3.7%)

4.3.2. Response surfaces

Fig. 21 depicts the 3D response surfaces for the two output parameters showing the visualized effects of input parameters in circular impinging jets. The minimum value point and region of each response surfaces are displayed as the red dot point or dashed line. It can be observed that the average temperature of the target surface (T_{ave}) decreases monotonically as the nozzle diameter (d_c and d_o) decreases, but in the case of jet-to-jet spacing (S), the T_{ave} decreases as it increases and has a minimum value at a point other than the upper bound. The maximum temperature difference (T_{dif}) has declined as the value of S increases and d_o decreases, and the distinct thing is that the location of the minimum value region is near the lower bound of d_c . Like a circular impinging jet, Fig. 22 illustrates the effects of design parameters of the elliptic impinging jets on the response surfaces. The tendency that the effects of input parameters to T_{ave} are similar to circular jet. As the nozzle size (a , AR , and d_c) smaller, T_{ave} is decreases and the minimum value exists near the upper bound of S and lower bound of a , AR , and d_c . As shown in Fig. 22(e) – (h), the T_{dif} decreases as the nozzle size increases, which tends to be opposite of the T_{ave} . Also, it is confirmed that the uniform cooling performance of the elliptic jet is obtained as S increases. Through the RSM analysis, the effects of design factors of elliptic and circular array impinging jets on output parameters is examined, but it is difficult to compare the importance of each design parameter. To figure out the significance of design parameters, the sensitivity analysis is performed in this study.



**Fig. 21. Response surface plots showing the effects of design parameters for circular jet array:
 (a, b) the average temperature (c, d) the maximum temperature difference.**

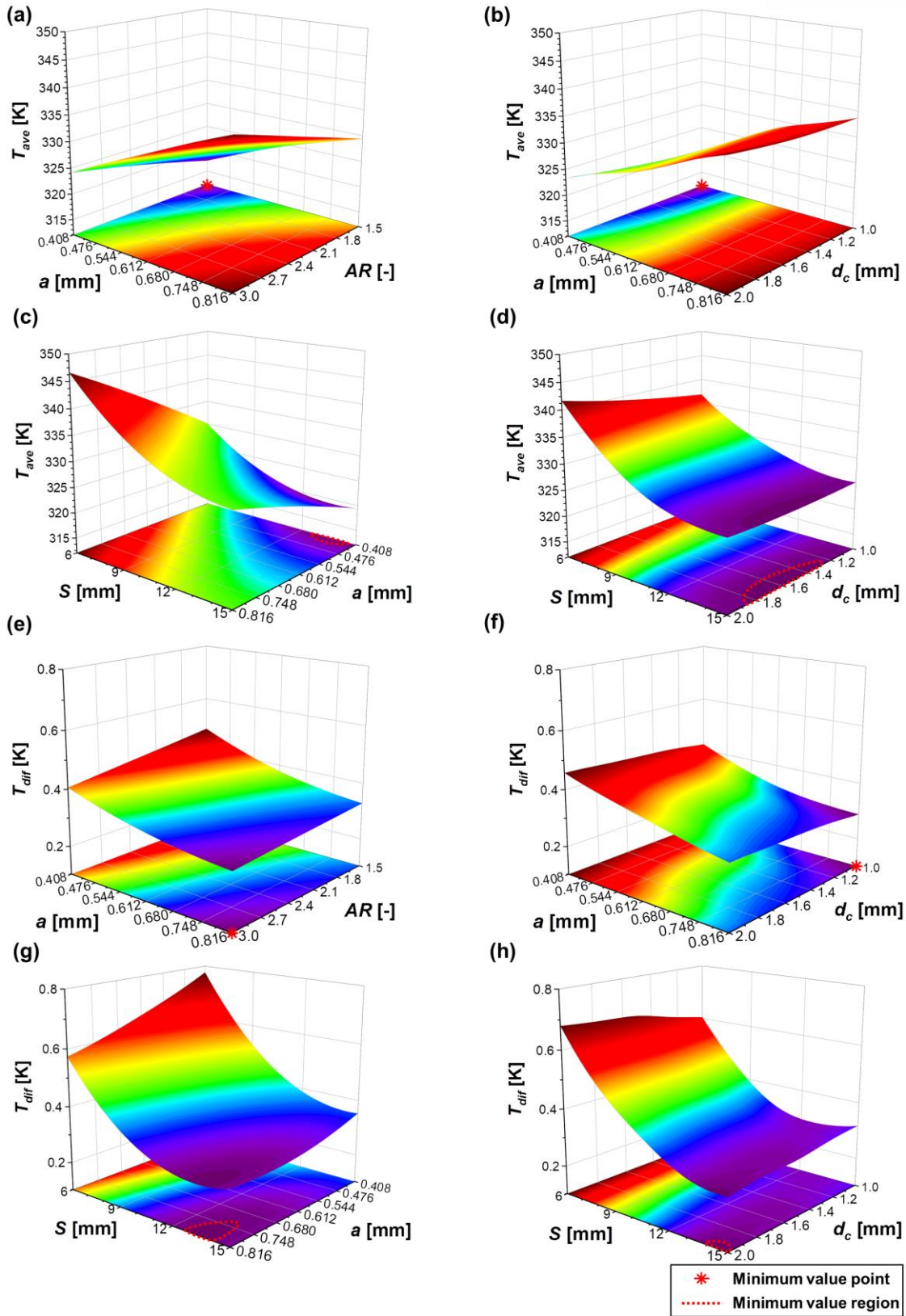


Fig. 22. Response surface plots showing the effects of design parameters for elliptic jet array: (a-d) the average temperature (e-h) the maximum temperature difference.

4.3.3. Sensitivity analysis

Sensitivity analysis can quantitatively evaluate the effects of design parameters on output parameters. It can be identified the major and minor design parameters on the cooling performance by comparing the sensitivity coefficients. Fig. 23 plots the sensitivity coefficients of the circular and elliptic jet array. A higher sensitivity coefficient means that the design parameters have a greater effect on the output parameters. In circular impinging jet, the central nozzle diameter (d_c) is a major parameter for T_{ave} and jet-to-jet spacing (S) is a major parameter for T_{dif} . The diameter of outer nozzles (d_o) has less effect on both T_{ave} and T_{dif} than other parameters. The negative value of the sensitivity coefficient means that the output parameter has decreased as the input parameter increases. In other words, in the case of S which has a negative value of sensitivity coefficient, T_{ave} and T_{dif} decrease as S increases. For the elliptic impinging jet array, S is a significant factor and the aspect ratio (AR) is a minor parameter for both T_{ave} and T_{dif} .

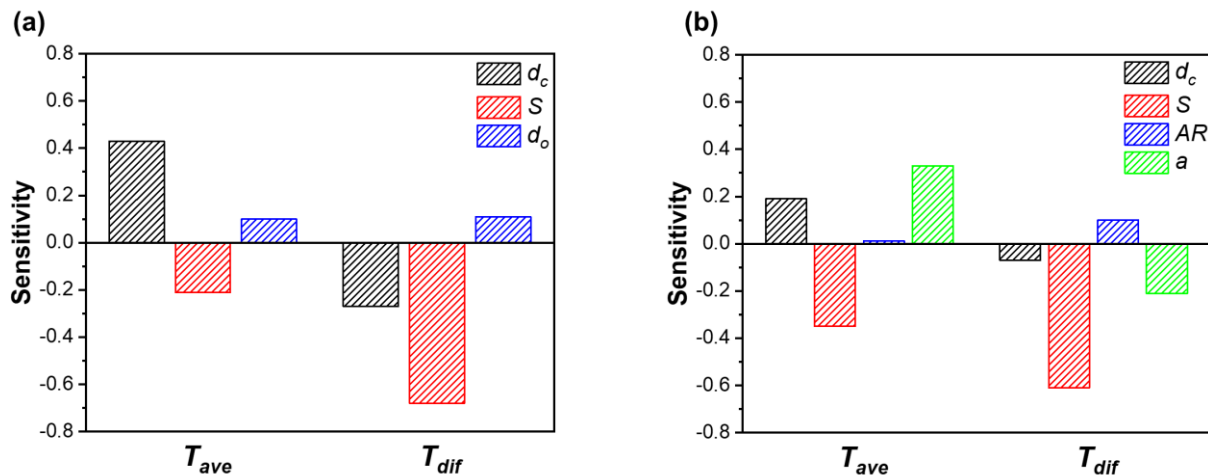


Fig. 23. The sensitivity of design parameters for (a) circular jet array (b) elliptic jet array.

4.3.4. Effect of S/D

Fig. 24 shows the velocity vector distributions which obtained at $S/D = 6.0$ and 15.0 . As soon as the jet issued from the nozzles, it undergoes the flow separation and enlargement due to the entrance of the surrounding fluid. As shown in Fig. 24(b), there is secondary stagnation region which ensures the uniform cooling of the target surface due to the jet-to-jet interactions between the adjacent jets [11]. After the collision between the wall jets, the fountain flow occurs and vortices (recirculation region) are formed around the jet-to-jet interaction region to both sides of central and outer nozzles. Depending on the strength of jet-to-jet interactions, the cooling characteristics of array jets are determined. The vigorous interactions can improve heat transfer rates. Contrary to the flow characteristics at $S/D = 15.0$, different flow patterns are shown at $S/D = 6.0$, as indicated in Fig. 24(b). At small S/D , the jet-to-jet interaction occurs prior to the jet impingement on the target surface, this phenomenon called jet interference. The jet interference disturbs the flow motions of jets, so it deteriorates the cooling performance of array impinging jet. Thus, the value of S/D is a significant factor affecting the cooling characteristics of array jets.

Fig. 25 illustrated the detailed maximum temperature difference (T_{dif}) distributions showing the temperature non-uniformity on the target surface with varying S/D . To compare the effects of S/D to the temperature distribution on impinging surface, the three values of S/D are adopted: (a) small $S/D = 6.0$, (b) intermediate $S/D = 10.5$, and (c) large $S/D = 15.0$. The value of T_{dif} is consistently increases as decreasing the S/D from 15.0 to 6.0 . There are mid-way regions where jet-to-jet interaction occurs in the case of $S/D = 10.5$, but not at $S/D = 6.0$, as compared by Fig. 25 (a) and (b). It is worth noting that an inflection point exists between the value of $S/D = 6.0$ to 10.5 that changes the phenomena from jet interference to jet-to-jet interaction. At the same value of S/D , the cooling characteristics of circular array nozzles arranged radial (CJ2) appears as the worst scenario among the optimum designs. The CJ2 array jets are still in the jet interference flow region despite the value of $S/D = 10.5$, which lags behind other optimum designs in cooling performance. The elliptic array nozzles arranged inline (EJ2) covers the broad area of the target surface than circular array nozzles arranged radial (CJ1), resulting in outperformed cooling performance.

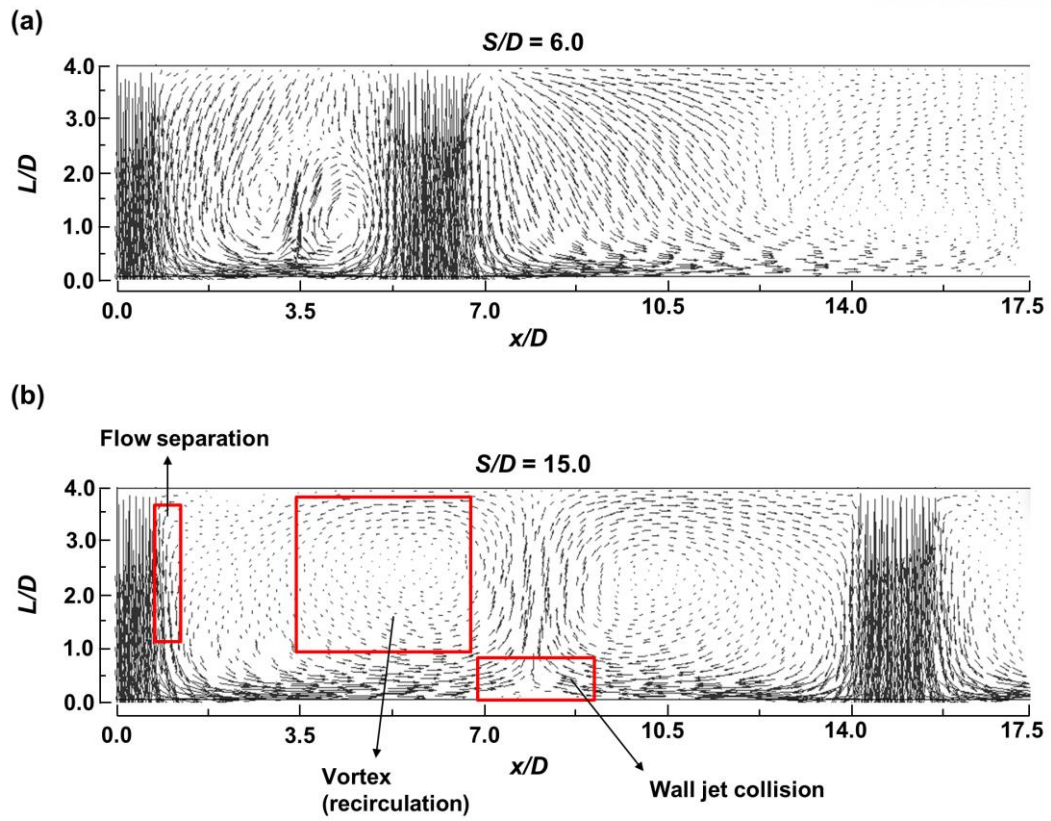


Fig. 24. Velocity vectors with different jet-to-jet spacings: (a) $S/D = 6.0$ (b) $S/D = 15.0$.

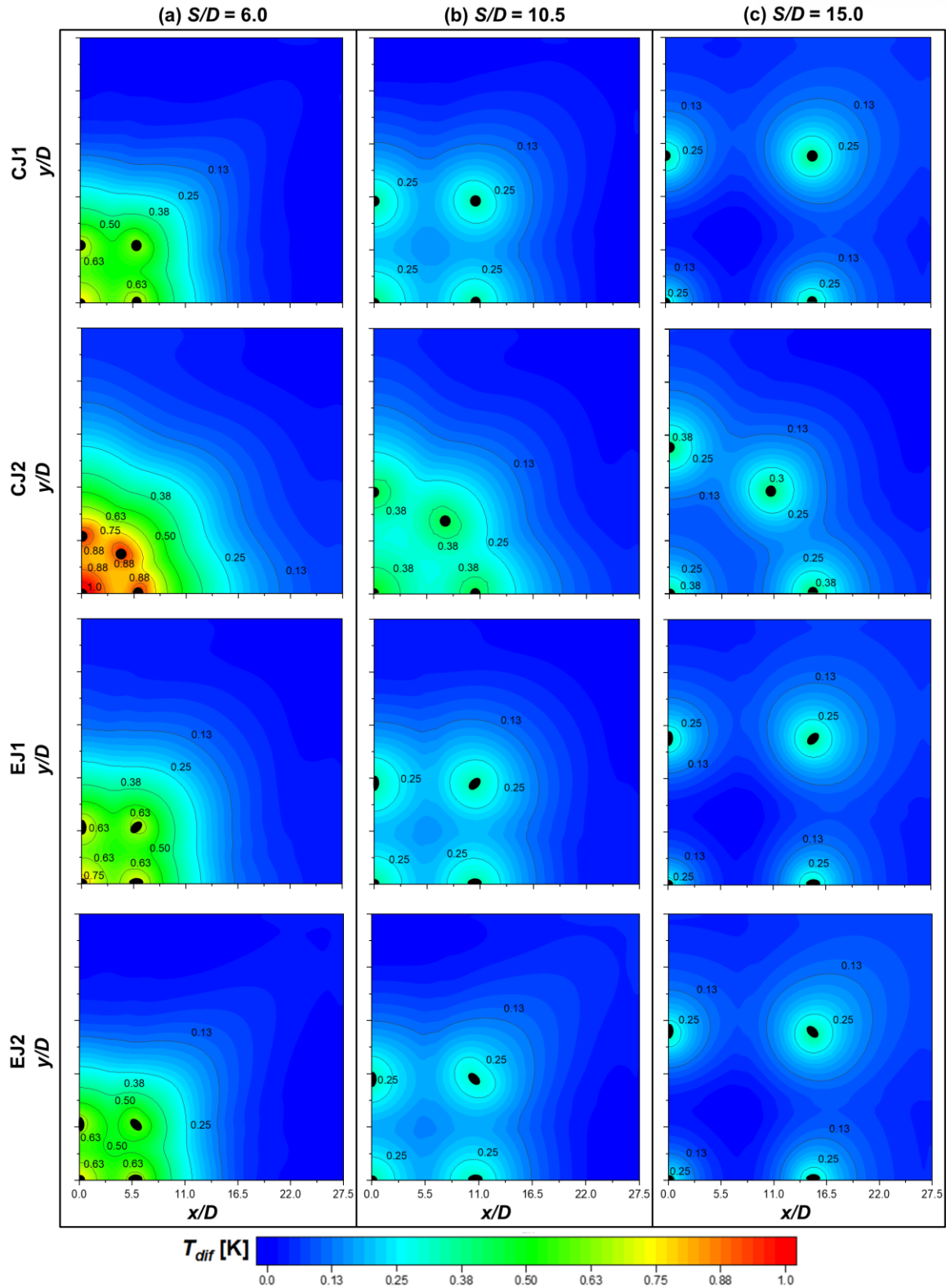


Fig. 25. The maximum temperature difference contours showing the temperature distributions on the cooling surface for the array impinging jets with varying jet-to-jet spacings: (a) $S/D = 6.0$ (b) $S/D = 10.5$ (c) $S/D = 15.0$.

4.3.5. Comparison of flow characteristics

Fig. 26 shows the axial velocity and turbulent kinetic energy (TKE) distributions at the location of jet center and jet-to-jet interaction, which locations are corresponding at $(x/D, z/D = 0.0, 15.0)$ and $(x/D, z/D = 0.0, 7.5)$, respectively. The v and V_j represents the axial velocity and velocity of nozzle inlet, and the velocity components are nondimensionalized by the nozzle inlet velocity. The CFD calculations of the circular and elliptic jet array (CJ and EJ) are performed at the equivalent diameter 1.0 mm, jet-to-jet spacing 15.0 mm, and the dimensionless nozzle-to-plate distance set as 4.0. As shown in Fig. 26(a) and (b), axial velocity distributions at the jet center do not differ considerably between the CJ and EJ, but a noticeable difference appeared in the jet interaction region. From Fig. 25(c) and (d), as can be seen in the TKE distributions which directly affects the thermal energy transfer, the TKE profiles of EJ has a superior to CJ, especially near the impinging plate. Summarizing the comparison of CJ and EJ, at the jet center, the flow characteristics of EJ are similar to those of CJ, but EJ surpasses CJ at the jet interaction region. Therefore, the elliptic jet array is more suitable for array impinging jet heat transfer than the circular impinging jet array.

The axial velocity and TKE profiles of CJ1, CJ2, EJ1, and EJ2 configurations at the jet center and interaction region are compared in Fig. 27. The location of the jet interaction region is selected based on the value of half the jet-to-jet spacing. As shown in Fig. 27(a) and (b), the axial velocity curves for all optimum designs of array jet have similar distributions, which means that the axial velocity profiles at the jet center are independent of nozzle geometry. However, there is big difference between the optimum configurations in the axial velocity of the jet interaction region, the highest axial velocity distributions are obtained for EJ2. Fig. 27(c) and (d) describes the TKE profiles at the location of jet center and interaction region. At the jet center, the TKE profiles of the circular jet array (CJ1 and CJ2) has a slightly lower than the elliptic jet array (EJ1 and EJ2). The TKE curves at the jet interaction region have a similar trend for all optimum designs, but the strength of TKE has a substantial difference. It is worth noting that the nozzle geometry is significantly affect the flow and heat transfer characteristics.

Fig. 28 represents the comparison of 3D streamlines between CJ1 and EJ2 configurations. For array impinging jets, the vortex rings are generated by the jet-to-jet interaction between adjacent jets. These vortex rings are significantly affecting the temperature distributions of target surface [45]. The large vortex ring means that the high strength of jet-to-jet interaction. It is observed that the EJ2 configuration has the larger vortex rings than CJ1 configuration. Furthermore, the jet velocity of EJ2 is higher than that of CJ1. Based on the results from the flow characteristics and 3D streamlines, it is confirmed that the elliptic jet arrays have outperformed than the circular jet array.

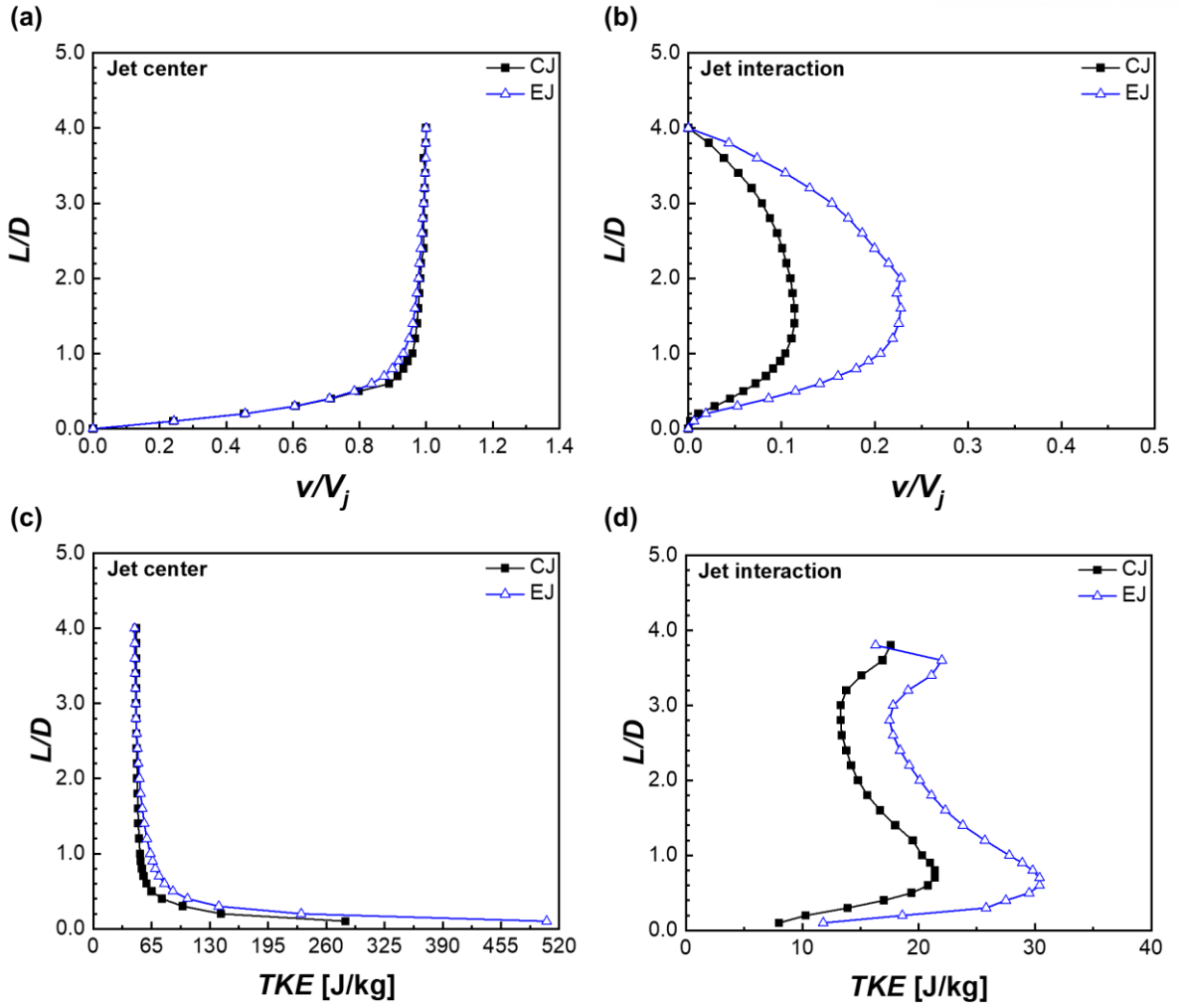


Fig. 26. Axial velocity and TKE distributions for CJ and EJ at the locations of jet center (a, c) jet-to-jet interaction (b, d).

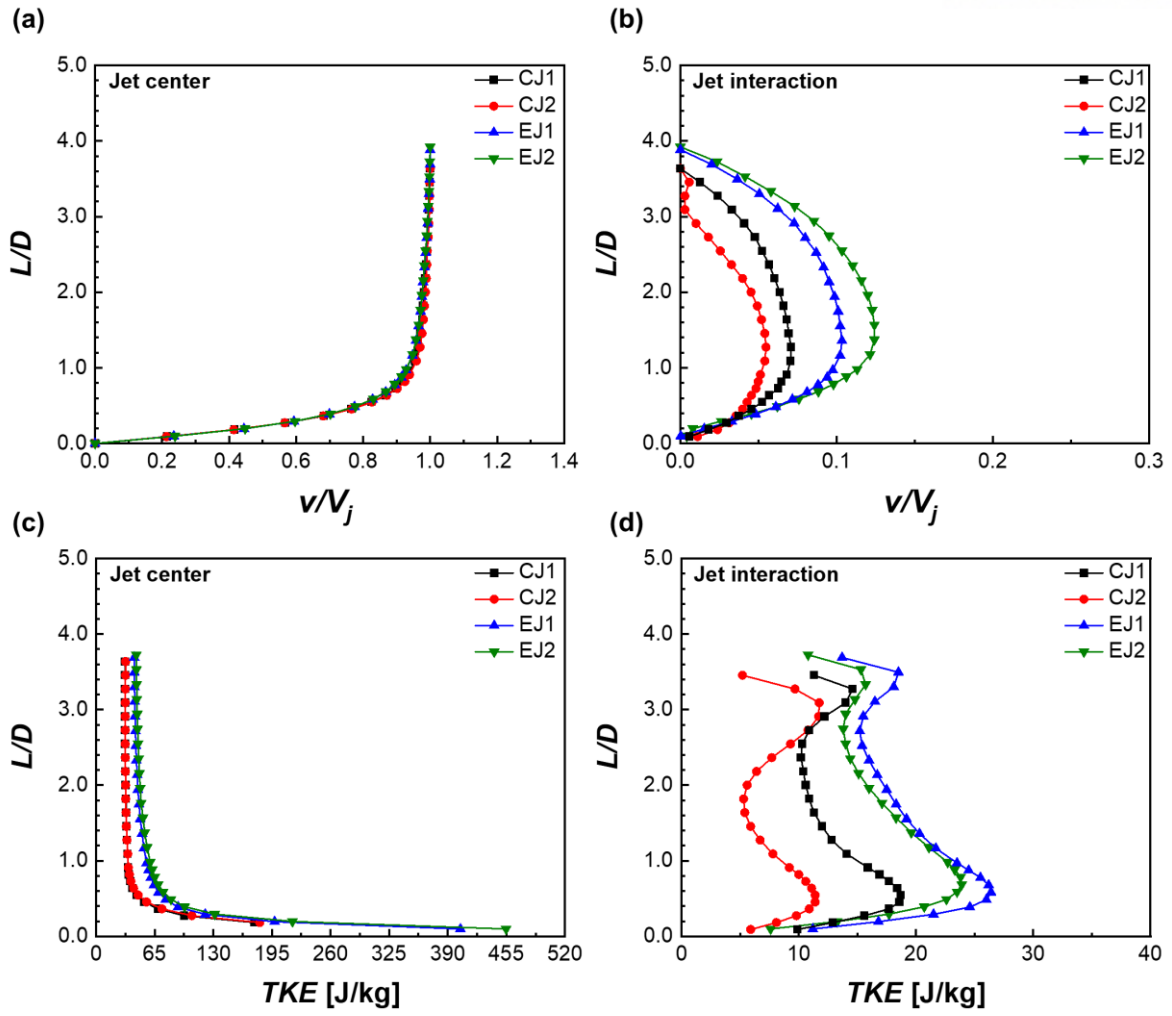
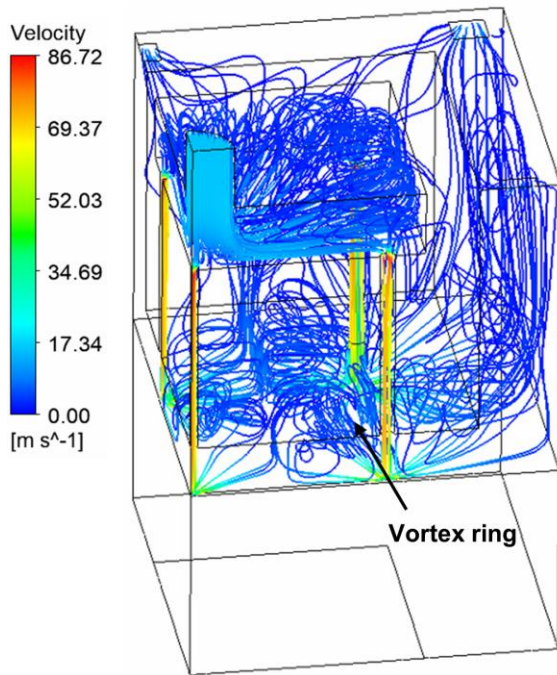


Fig. 27. Axial velocity and TKE distributions for CJ1, CJ2, EJ1, and EJ2 at the locations of jet center (a, c) jet-to-jet interaction (b, d).

(a) CJ1



(b) EJ2

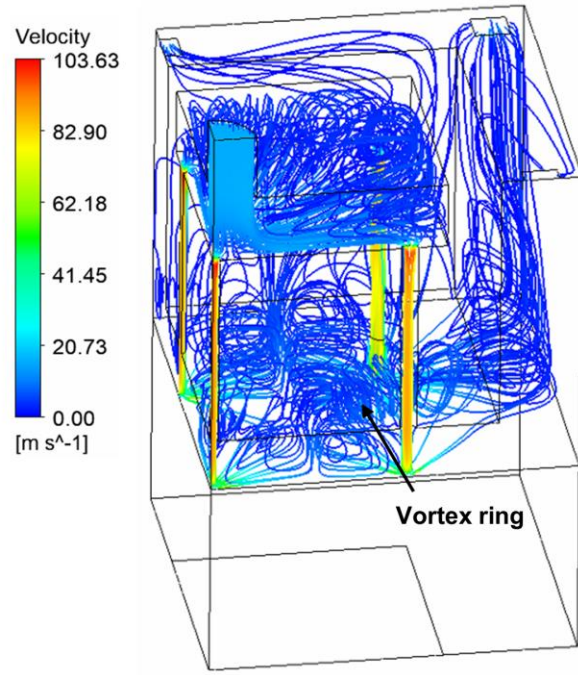


Fig. 28. Comparison of the 3D streamlines between CJ1 and EJ2 configurations.

4.3.6. 3D printed impinging jet arrays

Fig. 29 shows the 3D printed impinging jet array nozzles of optimum designs in CJ1, CJ2, EJ1, and EJ2, respectively. The design parameters of S , d_c , d_o , a , and AR denote the jet-to-jet spacing, central nozzle diameter, outer nozzle diameter, minor axis length, and aspect ratio, respectively. The configurations for CJ1 and CJ2 have the circular nozzles with the inline and radial arrangement. The optimum designs for EJ1 and EJ2 have a circular nozzle at the central of the jet array and elliptic nozzles at the outer of jet array with the inline arrangement.

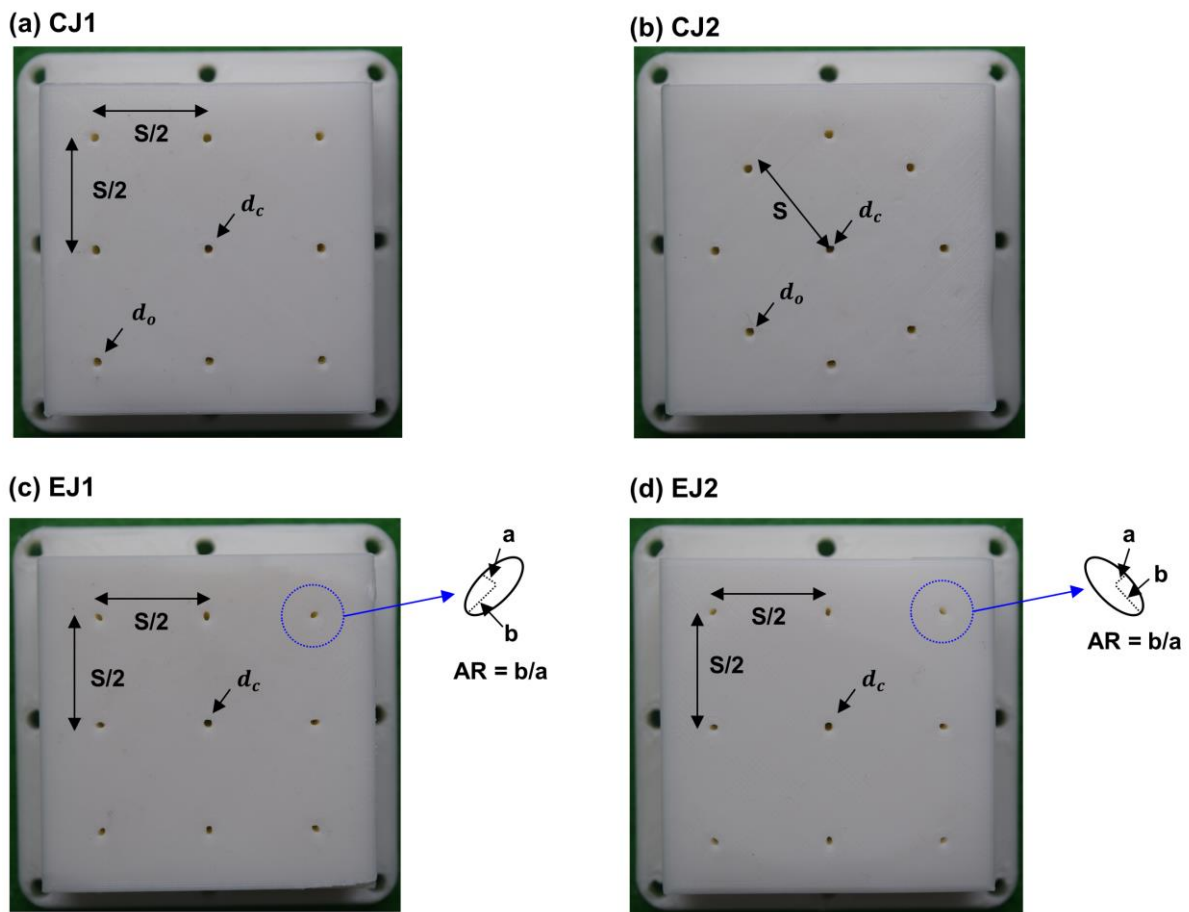


Fig. 29. The 3D printed impinging jet array nozzles of optimum design in CJ1, CJ2, EJ1, and EJ2, respectively.

4.3.7. Confirmation experiments

The verification experiments of optimization results are performed using the 3D printed impinging jet nozzles of optimum designs. The cooling performance of array impinging jets is evaluated at the nozzle-to-plate distance (L) in the range of 4.0 to 22.0 mm for the volume flow rate 30.0 to 80.0 LPM. The L is nondimensionalized by the equivalent diameter of the jet array.

Fig. 30 shows the measured stagnation temperature distributions of CO_2 impinging jets with varying L/D . The stagnation temperatures linearly decrease as L/D decreases over all optimum design configurations. This is because the jet velocity becomes decay as it moves away from the target surface due to the shear-driven interaction between the jet and ambient fluid. For the array impinging jets with $Re_D = 8,493$ using the EJ2 configuration, the stagnation temperature is decreased by about 4.75 K as the value of L/D decreases 21.5 to 3.9.

The effects of Re_D on the stagnation temperature with CO_2 array impinging jets at $L/D = 4.0$ are shown in Fig. 31. It is confirmed that the stagnation temperature decreases as the Re_D increases over all cases. At the low Reynolds number, there are no big differences in the stagnation temperature between the optimum designs except for ICJ. However, the differences are increasing as the Re_D increases, and the best scenario for impinging jet heat transfer is using the EJ2 configuration. These results imply that the high Re_D corresponds to a large amount of CO_2 impinging jets with lowered temperature due to the Joule-Thomson effect. Namely, the high Re_D ensures the lowered temperature of the target surface with enhanced cooling performance.

Fig. 32. Shows the comparative plots of experimentally and numerically obtained results on the cooling performance of impinging jet arrays. The experimental results agree well with the CFD predictions based on the average temperature of the target surface, as can be seen Fig. 32(a). Furthermore, the order of superior configurations of impinging jet arrays is agreed well with the order EJ2, EJ1, CJ1, and CJ2 of CFD predictions. Fig. 32(b) shows the comparison between CFD predictions and experiment results on the maximum temperature difference of target surface with a measurement error of thermocouple. It is confirmed that the maximum uncertainty of temperature difference is about ± 0.707 K by error propagation. As a result, it is difficult to measure the temperature non-uniformity of the target surface by experiment method. Although the reliability of the experiment results on the maximum temperature difference is low, CFD simulations confirmed that the optimum designs have a uniform cooling performance than the initial design. In conclusion, based on the CFD predictions and experiment results, it is confirmed that the best scenario for the array impinging jet heat transfer is the using the EJ2 jet configuration.

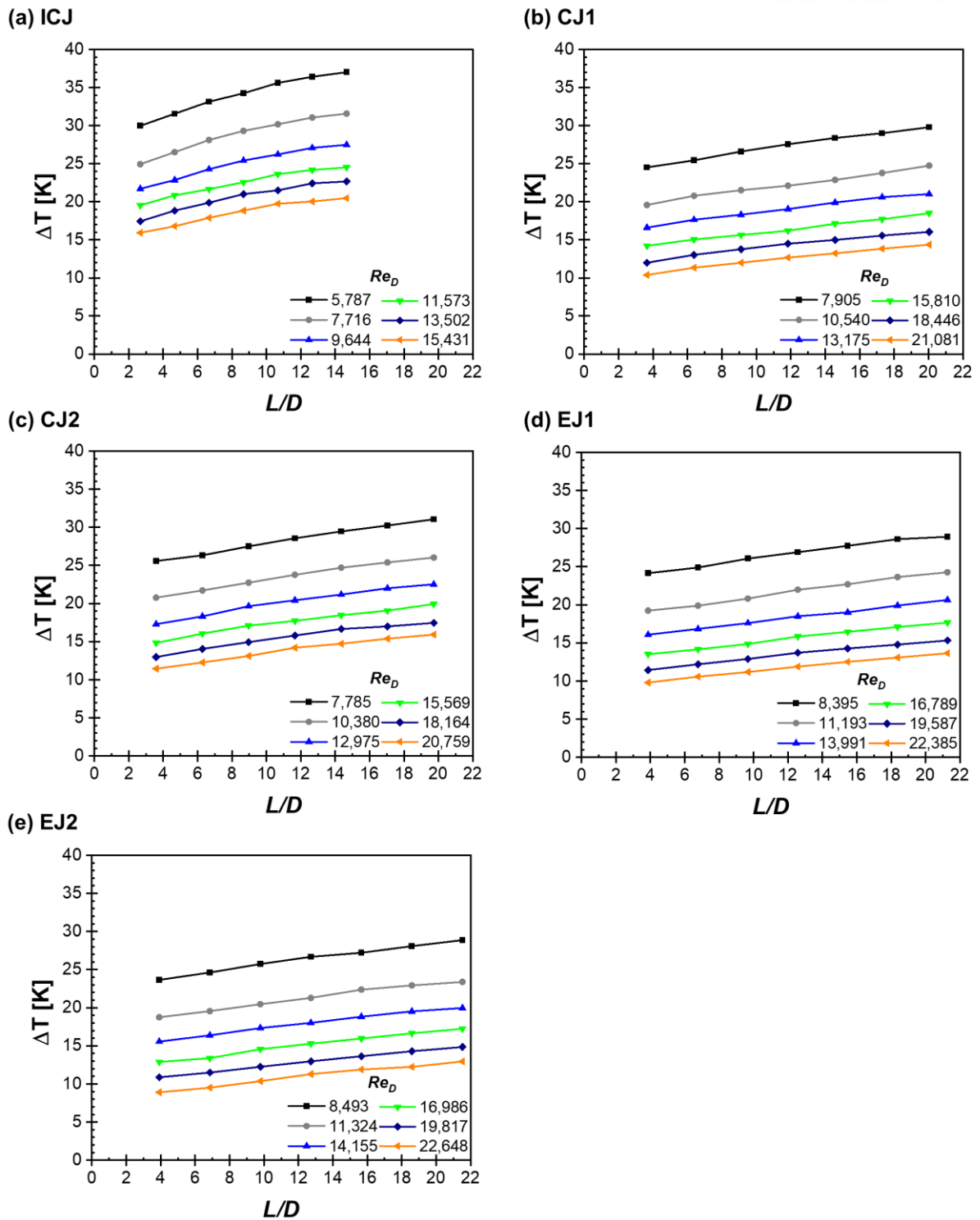


Fig. 30. The stagnation temperature distributions with varying L/D : (a) ICJ (b) CJ1 (c) CJ2 (d) EJ1 (e) EJ2.

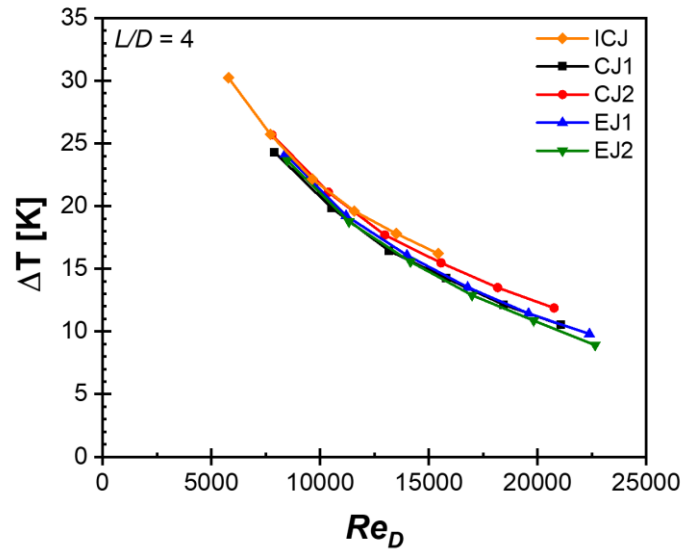


Fig. 31. The effects of Re_D on the stagnation temperature.

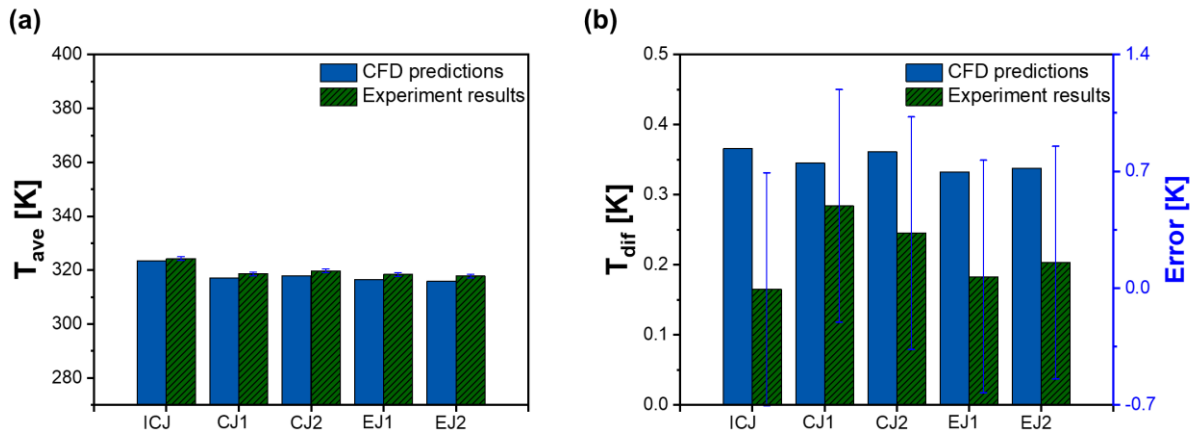


Fig. 32. The comparison between CFD predictions and experiment results: (a) average temperature (b) maximum temperature difference.

5. Conclusions

5.1. Part I: Cooling characteristics of single and array impinging jets

In Part I, the single and array impinging jet heat transfer with CO_2 and N_2 are experimentally performed compared with heat transfer coefficient and maximum temperature difference of test section varying with L/d and Re_D . The salient conclusions are listed below.

- (1) The temperature drop caused by nozzle expansion is about 3.49 °C and 0.64 °C under the condition of CO_2 jet (NPR=4.19) and N_2 jet (NPR=3.25), respectively.
- (2) Owing to the material properties of the PLA used for 3D printing, the correlations between the CAD design and measured dimensions of the structure are established to predict the shrinking of PLA due to thermal expansion. It is confirmed that the correlations for accurate 3D printed structures are well build based on the coefficient of determination (R^2).
- (3) There is maximum value of stagnation heat transfer coefficient at certain L/D . The value of L/D with the maximum heat transfer coefficient tends to increase as the Re_D increases, and the maximum value of single CO_2 impinging jet is more clearly distinguished than single N_2 impinging jet. This trend is due to the larger temperature drop of CO_2 jet as the Re_D increases.
- (4) The heat transfer coefficient of CO_2 impinging jet is more sensitive of Re_D increasing than that of N_2 impinging jet. In case of same Re_D , the heat transfer coefficient of N_2 impinging jet is higher than CO_2 . However, in case of same volume flow rate, the heat transfer coefficient of CO_2 is superior to N_2 . These phenomena due to the difference in the thermal properties that affect the Re_D , such as the viscosity of the CO_2 and N_2 . Under the same experimental conditions, cooling performance of CO_2 is always higher than that of N_2 .
- (5) The performance of uniform cooling of CO_2 and N_2 array impinging jet has a similar level. However, there is a big difference in the average temperature of the test section, so it is beneficial to use the array CO_2 impinging jet for guarantee both high heat transfer coefficient and lowered temperature non-uniformity.

5.2. Part II: Geometry optimization and verification experiments

In Part II, the geometry optimization of array CO_2 impinging jet is performed to achieve the enhanced cooling performance using the RSM and MOGA approach. The effects of design parameters (S , d_c , d_o , a , AR) are analyzed. Also, the cooling performance are evaluated based on T_{ave} and T_{dif} . Furthermore, the verification experiments of optimization results are performed by using FDM 3D printing technique. The key conclusions are listed below.

- (1) The non-dominated optimal solutions of the multi-objective problem, Pareto-front, are obtained using MOGA model based on NSGA-II. The predicted error between the candidate of the optimal solution and real solve is less than 5 % in all cases. Compared with the initial design, it is confirmed that in the case of EJ2, the T_{ave} and T_{dif} (temperature non-uniformity) is improved by about 7.6 K and 7.7 %. The cooling performance of the elliptic jet array surpasses the circular jet array, the best scenario is for EJ2 and worst is for CJ2.
- (2) The visualized effects of design parameters to output parameters are illustrated by the 3D response surface. The main trend is that as nozzle size smaller, the T_{ave} decreases and T_{dif} increases. In addition, as the jet-to-jet spacing (S) increases, the T_{ave} and T_{dif} are decreases. The significance of design parameters is evaluated by sensitivity analysis. For the CJ, the d_c and S are major parameters on the T_{ave} and T_{dif} , respectively. In the case of EJ, the value of S is the major parameter for both T_{ave} and T_{dif} .
- (3) The effects of S/D are analyzed by compared the velocity vector distributions and maximum temperature difference contours. At small S/D , the jet interference that the jets are disturbed by adjacent jets before impinging on the target surface have occurred. The jet interference deteriorates the heat transfer rates of array jets. At $S/D= 10.5$, the optimum designs are beyond the jet interference effects except for CJ2.
- (4) The flow characteristics of optimum configurations are evaluated at the location of the jet center and jet interaction. It is confirmed that the axial velocity and turbulent kinetic energy (TKE) distributions of the EJ are superior to CJ at the jet interaction region. As a result, the cooling performance of the elliptic array impinging jet outperformed than circular array impinging jet.
- (5) The cooling performance of array impinging jets is evaluated with varying L/D and Re_D . For all optimum configurations of the jet array, the stagnation temperatures linearly decrease as L/D decreases. The stagnation temperature decreases as the Re_D increases. This result indicates that the high Reynolds number ensures a large amount of CO_2 impinging jets with lowered temperature due to the Joule-Thomson effect.

- (6) The experimental results are matched well with the CFD predictions based on the average temperature (T_{ave}). Moreover, the order of superior geometries on the array impinging jet heat transfer is agreed well with the order EJ2, EJ1, CJ1, and CJ2 of CFD predictions. It is observed that the maximum temperature difference (T_{dif}) of the target surface is difficult to measure by the experiment method due to its uncertainty error is exceed the order of T_{dif} . Although the reliability of the experimental results for the T_{dif} is low, CFD predictions confirmed that the optimum designs have a uniform cooling performance than the initial designs.

REFERENCES

- [1] S. W. Chang, S. F. Chiou, and S. F. Chang, "Heat transfer of impinging jet array over concave-dimpled surface with applications to cooling of electronic chipsets," *Exp. Therm. Fluid Sci.*, vol. 31, no. 7, pp. 625–640, 2007.
- [2] K. S. Choo and S. J. Kim, "Comparison of thermal characteristics of confined and unconfined impinging jets," *Int. J. Heat Mass Transf.*, vol. 53, no. 15–16, pp. 3366–3371, 2010.
- [3] J. C. Kurnia, A. P. Sasmito, P. Xu, and A. S. Mujumdar, "Performance and potential energy saving of thermal dryer with intermittent impinging jet," *Appl. Therm. Eng.*, vol. 113, pp. 246–258, 2017.
- [4] K. Nakabe, K. Inaoka, T. Ai, and K. Suzuki, "Flow visualization of longitudinal vortices induced by an inclined impinging jet in a crossflow-effective cooling of high temperature gas turbine blades," *Energy Conversion and Management*, vol. 38, no. 13–10, pp. 1145–1153, 1997.
- [5] N. NITIN and M. V. KARWE, "Numerical Simulation and Experimental Investigation of Conjugate Heat Transfer between a Turbulent Hot Air Jet Impinging on a Cookie-shaped Object," *J. Food Sci.*, vol. 69, no. 2, pp. fep59–fep65, 2006.
- [6] J.-C. Han, "Recent Studies in Turbine Blade Cooling," *Int. J. Rotating Mach.*, vol. 10, no. 6, pp. 443–457, 2004.
- [7] F. Wan, Y. qin Wang, and S. ren Qin, "Modeling of Strip Temperature in Rapid Cooling Section of Vertical Continuous Annealing Furnace," *J. Iron Steel Res. Int.*, vol. 19, no. 11, pp. 27–32, 2012.
- [8] F. Monnoyer and D. Lochegnies, "Heat transfer and flow characteristics of the cooling system of an industrial glass tempering unit," *Appl. Therm. Eng.*, vol. 28, no. 17–18, pp. 2167–2177, 2008.
- [9] Z. Ling *et al.*, "Review on thermal management systems using phase change materials for electronic components, Li-ion batteries and photovoltaic modules," *Renew. Sustain. Energy Rev.*, vol. 31, pp. 427–438, 2014.
- [10] J. Lee and S. J. Lee, "Stagnation region heat transfer of a turbulent axisymmetric jet impingement," *Exp. Heat Transf.*, vol. 12, no. 2, pp. 137–156, 1999.
- [11] B. Weigand and S. Spring, "Multiple Jet Impingement - A Review," *Heat Transf. Res.*, vol. 42, no. 2, pp. 101–142, 2011.
- [12] P. Hrycak, D.T. Lee, J.W. Gauntner, J.N.B. Livingood, "Experimental Flow Characteristics of a Single Turbulent Jet Impinging on a Flat Plate," *Nasa Tn D-5690*, 1970.

- [13] K. Kataoka, “Optimal Nozzle-To-Plate Spacing for Convective Heat Transfer in Nonisothermal, Variable-Density Impinging Jets,” *Dry. Technol.*, vol. 3, no. 2, pp. 235–254, 1985.
- [14] T. Guo, M. J. Rau, P. P. Vlachos, and S. V. Garimella, “Axisymmetric wall jet development in confined jet impingement,” *Phys. Fluids*, vol. 29, no. 2, 2017.
- [15] V. Katti and S. V. Prabhu, “Experimental study and theoretical analysis of local heat transfer distribution between smooth flat surface and impinging air jet from a circular straight pipe nozzle,” *Int. J. Heat Mass Transf.*, vol. 51, no. 17–18, pp. 4480–4495, 2008.
- [16] B. Yang, S. Chang, H. Wu, Y. Zhao, and M. Leng, “Experimental and numerical investigation of heat transfer in an array of impingement jets on a concave surface,” *Appl. Therm. Eng.*, vol. 127, pp. 473–483, 2017.
- [17] J. Y. San and J. J. Chen, “Effects of jet-to-jet spacing and jet height on heat transfer characteristics of an impinging jet array,” *Int. J. Heat Mass Transf.*, vol. 71, pp. 8–17, 2014.
- [18] Y. Xing, S. Spring, and B. Weigand, “Experimental and numerical investigation of heat transfer characteristics of inline and staggered arrays of impinging jets,” *J. Heat Transfer*, vol. 132, no. 9, pp. 1–11, 2010.
- [19] M. Wae-hayee, K. Yeranee, I. Piya, Y. Rao, and C. Nuntadusit, “Heat transfer correlation of impinging jet array from pipe nozzle under fully developed flow,” *Appl. Therm. Eng.*, vol. 154, no. October 2018, pp. 37–45, 2019.
- [20] B. P. E. Dano, J. A. Liburdy, and K. Kanokjaruvijit, “Flow characteristics and heat transfer performances of a semi-confined impinging array of jets: Effect of nozzle geometry,” *Int. J. Heat Mass Transf.*, vol. 48, no. 3–4, pp. 691–701, 2005.
- [21] P. Culun, N. Celik, and K. Pihtili, “Effects of design parameters on a multi jet impinging heat transfer,” *Alexandria Eng. J.*, vol. 57, no. 4, pp. 4255–4266, 2018.
- [22] S. Caliskan, S. Baskaya, and T. Calisir, “Experimental and numerical investigation of geometry effects on multiple impinging air jets,” *Int. J. Heat Mass Transf.*, vol. 75, pp. 685–703, 2014.
- [23] M. Attalla, H. M. Maghrabie, A. Qayyum, A. G. Al-Hasnawi, and E. Specht, “Influence of the nozzle shape on heat transfer uniformity for in-line array of impinging air jets,” *Appl. Therm. Eng.*, vol. 120, pp. 160–169, 2017.
- [24] J. Lee and S. J. Lee, “The effect of nozzle aspect ratio on stagnation region heat transfer characteristics of elliptic impinging jet,” *Int. J. Heat Mass Transf.*, vol. 43, no. 4, pp. 555–575, 2000.
- [25] P. Gulati, V. Katti, and S. V. Prabhu, “Influence of the shape of the nozzle on local heat transfer distribution between smooth flat surface and impinging air jet,” *Int. J. Therm. Sci.*, vol. 48, no. 3, pp. 602–617, 2009.

- [26] M. F. Koseoglu and S. Baskaya, “The role of jet inlet geometry in impinging jet heat transfer, modeling and experiments,” *Int. J. Therm. Sci.*, vol. 49, no. 8, pp. 1417–1426, 2010.
- [27] P. Zhang, G. H. Xu, X. Fu, and C. R. Li, “Confined jet impingement of liquid nitrogen onto different heat transfer surfaces,” *Cryogenics*, vol. 51, no. 6, pp. 300–308, 2011.
- [28] D. Kim and J. Lee, “Experimental investigation of CO₂ dry-ice assisted jet impingement cooling,” *Appl. Therm. Eng.*, vol. 107, pp. 927–935, 2016.
- [29] S. Kwak and J. Lee, “Eulerian multiphase analysis for heat transfer enhancement by CO₂ sublimation in slot jet impingement,” *Int. J. Multiph. Flow*, vol. 107, pp. 182–191, 2018.
- [30] Z. Chi, H. Liu, and S. Zang, “Geometrical optimization of nonuniform impingement cooling structure with variable-diameter jet holes,” *Int. J. Heat Mass Transf.*, vol. 108, pp. 549–560, 2017.
- [31] K. T. Chiang, “Modeling and optimization of designing parameters for a parallel-plain fin heat sink with confined impinging jet using the response surface methodology,” *Appl. Therm. Eng.*, vol. 27, no. 14–15, pp. 2473–2482, 2007.
- [32] M. W. Heo, K. D. Lee, and K. Y. Kim, “Optimization of an inclined elliptic impinging jet with cross flow for enhancing heat transfer,” *Heat Mass Transf.*, vol. 47, no. 6, pp. 731–742, 2011.
- [33] D. L. A. Fernandes, M. V. Pavliuk, and J. Sá, “A 3D printed microliquid jet with an adjustable nozzle diameter,” *Analyst*, vol. 140, no. 18, pp. 6234–6238, 2015.
- [34] A.U.M. Masuk, A. Salibindla, S. Tan, and R. Ni, “V-ONSET (Vertical Octagonal Noncorrosive Stirred Energetic Turbulence): A vertical water tunnel with a large energy dissipation rate to study bubble/droplet deformation and breakup in strong turbulence,” *Rev. Sci. Instrum.*, vol. 90, no. 8, 2019.
- [35] N.V.S. Shankar and H. R. Shankar, “Heat transfer during multi swirl jet impingement: Experimentation,” *Int. J. Mech. Eng. Technol.*, vol. 9, no. 11, pp. 493–499, 2018.
- [36] T. W. Wei, H. Oprins, V. Cherman, E. Beyne, and M. Baelmans, “Experimental and numerical investigation of direct liquid jet impinging cooling using 3D printed manifolds on lidded and lidless packages for 2.5D integrated systems,” *Appl. Therm. Eng.*, vol. 164, no. October 2019, p. 114535, 2020.
- [37] C. M. Oldenburg, “Joule-Thomson cooling due to CO₂ injection into natural gas reservoirs,” *Energy Convers. Manag.*, vol. 48, no. 6, pp. 1808–1815, 2007.
- [38] Lemmon, E.W., Huber, M.L., McLinden, M.O. NIST Standard Reference Database 23: Reference Fluid Thermodynamic and Transport Properties-REFPROP, Version 9.1, *National Institute of Standards and Technology, Standard Reference Data Program, Gaithersburg*, 2013.
- [39] K. Olesen, R. Bredtmann, and R. Eisele, “ShowerPower New Cooling Concept for Automotive Applications,” *Automot. Power Electron.*, no. June, pp. 1–9, 2006.

- [40] Y. Han, B. L. Lau, G. Tang, X. Zhang, and D. M. W. Rhee, “Si-Based Hybrid Microcooler with Multiple Drainage Microtrenches for High Heat Flux Cooling,” *IEEE Trans. Components, Packag. Manuf. Technol.*, vol. 7, no. 1, pp. 50–57, 2017.
- [41] J. Jörg, S. Taraborrelli, G. Sarriegui, R. W. De Doncker, R. Kneer, and W. Rohlf, “Direct single impinging jet cooling of a mosfet power electronic module,” *IEEE Trans. Power Electron.*, vol. 33, no. 5, pp. 4224–4237, 2018.
- [42] G. Natarajan and R. J. Bezama, “Microjet cooler with distributed returns,” *Heat Transf. Eng.*, vol. 28, no. 8–9, pp. 779–787, 2007.
- [43] S. N. H. Mazlan, M. R. Alkahari, F. R. Ramli, M. N. Sudin, N. A. Maidin, and O. K. Sun, “Manufacturability of mechanical structure fabricated using entry level 3D printer,” *J. Mech. Eng.*, vol. 5, no. Specialissue3, pp. 98–122, 2018.
- [44] J. Y. San, C. H. Huang, and M. H. Shu, “Impingement cooling of a confined circular air jet,” *Int. J. Heat Mass Transf.*, vol. 40, no. 6, pp. 1355–1364, 1997.
- [45] M. D. Fox, M. Kurosaka, L. Hedges, and K. Hirano, “The influence of vortical structures on the thermal fields of jets,” *J. Fluid Mech.*, vol. 255, no. 6, pp. 447–472, 1993.
- [46] C. O. Popiel and O. Trass, “Visualization of a free and impinging round jet,” *Exp. Therm. Fluid Sci.*, vol. 4, no. 3, pp. 253–264, 1991.
- [47] B.E. Launder and D.B. Spalding, “Lectures in Mathematical Models of Turbulence”, *Academic Press*, London, 1972.
- [48] Y. Li, B. Li, F. Qi, and S. C. P. Cheung, “Flow and heat transfer of parallel multiple jets obliquely impinging on a flat surface,” *Appl. Therm. Eng.*, vol. 133, no. September 2017, pp. 588–603, 2018.
- [49] Y. Ozmen and G. Ipek, “Investigation of flow structure and heat transfer characteristics in an array of impinging slot jets,” *Heat Mass Transf.*, vol. 52, no. 4, pp. 773–787, 2016.
- [50] X. Yu, T. Chen, Q. Zhang, and T. Wang, “CFD simulations of quenching process for partial oxidation of methane: Comparison of jet-in-cross-flow and impinging flow configurations,” *Chinese J. Chem. Eng.*, vol. 26, no. 5, pp. 903–913, 2018.
- [51] M. Wolfshtein, “The velocity and temperature distribution in one-dimensional flow with turbulence augmentation and pressure gradient,” *Int. J. Heat Mass Transf.*, vol. 12, no. 3, pp. 301–318, 1969.
- [52] B. A. Kader, “Temperature and concentration profiles in fully turbulent boundary layers,” *Int. J. Heat Mass Transf.*, vol. 24, no. 9, pp. 1541–1544, 1981.
- [53] G. E. P. Box and K. B. Wilson, “On the experimental attainment of optimum conditions,” *J. Roy. Stat. Soc. B*, vol. 13, no. 1, pp. 1–38, 1951.

- [54] Z. Chi, H. Liu, and S. Zang, “Geometrical optimization of nonuniform impingement cooling structure with variable-diameter jet holes,” *Int. J. Heat Mass Transf.*, vol. 108, pp. 549–560, 2017.
- [55] A. Konak, D. W. Coit, and A. E. Smith, “Multi-objective optimization using genetic algorithms: A tutorial,” *Reliab. Eng. Syst. Saf.*, vol. 91, no. 9, pp. 992–1007, 2006.
- [56] D. H. Lee, J. Song, and M. C. Jo, “The effects of nozzle diameter on impinging jet heat transfer and fluid flow,” *J. Heat Transfer*, vol. 126, no. 4, pp. 554–557, 2004.
- [57] R. Vinze, S. Chandel, M. D. Limaye, and S. V. Prabhu, “Influence of jet temperature and nozzle shape on the heat transfer distribution between a smooth plate and impinging air jets,” *Int. J. Therm. Sci.*, vol. 99, pp. 136–151, 2016.
- [58] Z. X. Wen, Y. L. He, X. W. Cao, and C. Yan, “Numerical study of impinging jets heat transfer with different nozzle geometries and arrangements for a ground fast cooling simulation device,” *Int. J. Heat Mass Transf.*, vol. 95, pp. 321–335, 2016.

ACKNOWLEDGEMENTS

I had a lot of difficulties carrying out my research during master's course, but I am glad to be able to complete M.S. degree successfully. Above all, I would like to thank my advisor, Prof. Jaeseon Lee, for his enthusiasm, motivation, encouragement, and guidance on my research.

I would like to express my heartiest gratitude to my thesis committee, Prof. Jae Hwa Lee and Prof. Joo Hwan Oh, for their insightful comments and guidance on my thesis.

I would also like to thank my laboratory members who helped me with their fresh ideas.

I thank my family for their unconditional support throughout graduate school.

Last but not least, I'm grateful to those who didn't mention the name for their great support in my research.

Jaesik Lim

